THE ASTROPHYSICAL JOURNAL, 550:104–121, 2001 March 20
© 2001. The American Astronomical Society. All rights reserved. Printed in U.S.A.

MOLECULAR GAS IN OPTICALLY SELECTED MERGERS

MIN S. YUN[1]
National Radio Astronomy Observatory, P.O. Box O, Socorro, NM 87801-0387; myun@nrao.edu
AND
J. E. HIBBARD
National Radio Astronomy Observatory, 520 Edgemont Road, Charlottesville, VA 22903-2475; jhibbard@nrao.edu
Received 1999 March 26; accepted 2000 October 20

ABSTRACT

We have mapped the 2.6 mm CO $J = 1 \rightarrow 0$ emission in three optically selected "Toomre sequence" mergers (NGC 520, NGC 3921, NGC 4676). The molecular gas distribution is well resolved by the observations. For NGC 520 and NGC 4676A, the nuclear gas concentrations form a disklike or a ring-like structure, and the gas kinematics are regular and consistent with simple rotation. Discrete molecular gas complexes are found along the stellar bar in NGC 4676B, and the gas kinematics is consistent with the disk rotation traced in Hα. The molecular gas distribution in NGC 3921 is asymmetric about the stellar remnant, and both the distribution and kinematics suggest that the molecular gas has not settled into the center of the remnant. Molecular gas clouds are detected outside the central regions of NGC 3921 and NGC 4676, and they may be associated with the tidal tails and bridges mapped in H I. Departures from the canonical scenario for a merger involving two large spiral galaxies are found in all three Toomre sequence mergers studied. Our data suggest that one of the progenitor disks in NGC 520 and NGC 3921 was relatively gas-poor. A detailed comparison of these optically selected mergers and more luminous IR-selected mergers is deferred to a separate paper.

Subject headings: galaxies: individual (NGC 520, NGC 3921, NGC 4676) — galaxies: interactions — galaxies: ISM — infrared: galaxies

1. INTRODUCTION

It is widely believed that a physical collision between a pair of gas-rich galaxies leads to the concentration of gas and an intense starburst in the central region of the merger remnant (Toomre & Toomre 1972; Negroponte & White 1983). Indeed, the majority of infrared-bright galaxies are strongly disturbed systems, and massive concentrations of molecular gas have been detected in their central regions (see review by Sanders & Mirabel 1996 and references therein). However, this is not a complete and general picture of all galaxy collisions since many optically disturbed systems do not show strongly increased levels of massive star formation (Bushouse, Werner, & Lamb 1988). The majority of recent studies have focused mainly on infrared (IR) selected galaxies, and information on the molecular gas content and distribution within merging systems of modest IR luminosity is sparse in comparison.

A wide range of explanations is possible for the relatively modest levels of star-forming activity observed in the optically selected colliding galaxies. Unlike the IR-luminous systems, the progenitor disks of these systems may have been relatively gas-poor. Alternatively, the progenitors may have been gas-rich, but the initial conditions of the collisions were such that the bulk of the gas may have turned into stars or dispersed during the collision (e.g., Mihos & Hernquist 1996). It is also possible that the IR-luminous phase is generic but brief so that the less luminous mergers are seen in the pre- or postburst phase in their evolution.

As a first step in investigating these possible scenarios, we have used the Owens Valley Radio Observatory (OVRO) Millimeter Array to map the 2.6 mm CO $J = 1 \rightarrow 0$ transition line emission in three "Toomre sequence" mergers: NGC 520, NGC 3921, and NGC 4676. The "Toomre sequence" is an optically selected ensemble of strongly interacting galaxies representing a suggested evolutionary sequence of disk-disk mergers based on their stellar tidal tail lengths and the separation of the two nuclei (Toomre 1977). Since the members of this sequence were selected on the basis of optical morphology alone, they are much less biased toward systems with very high star formation rates than IR-selected samples.

The new high-resolution interferometric CO observations allow us to map the distribution and kinematics of the molecular gas in order to investigate the response of the molecular material that was previously distributed in the inner disks of the progenitors. These data are compared with existing high-resolution interferometric CO observations of IR-luminous mergers in a separate paper (Yun & Hibbard 2001, hereafter Paper II). In particular, we address whether any systematic difference exists in the properties of the molecular gas (which directly fuels the starburst activity) between the less luminous mergers and the IR-selected mergers that may explain the differences in the IR (and total) luminosity.

In § 2 we describe the three Toomre sequence mergers selected for this study. The details of the observations and data reduction are discussed in § 3. The results are described individually for each system in § 4, and a discussion of these results follows in § 5. Finally, in § 6 we summarize our conclusions.

2. SAMPLE SELECTION

The Toomre sequence consists of "eleven NGC prospects for ongoing mergers," as sketched and presented by Toomre (1977). The sequence was arranged based on the results of simple numerical simulations conducted by Toomre & Toomre (1972), which demonstrated the effects of bound

[1] Present address: University of Massachusetts, Astronomy Department, Amherst, MA 01003; myun@astro.umass.edu.

gravitational interactions on the outer regions of disk galaxies. This seminal work illustrated that long filamentary features are the natural consequence of the tidal forces experienced during such encounters, at the rate of one tail per prograde disk. Although their numerical technique did not allow for the inclusion of orbital decay, Toomre & Toomre (1972) posited that such decay should occur, thereby leading to the eventual merging of the participants. This proposal has been confirmed repeatedly with more sophisticated numerical treatments (see Barnes & Hernquist 1992, 1996; Barnes 1998 and references therein). The natural consequence of such encounters, the Toomres hypothesized, would be pairs of galaxies spiraling ever closer together, eventually leaving a single stellar body with two protruding tidal tails. The Toomre sequence was meant to depict this proposed evolutionary sequence of disk-disk mergers.

Four members of the Toomre sequence have been mapped previously in CO with the OVRO interferometer (NGC 4038/39 by Stanford et al. 1990 and Wilson et al. 2000; NGC 520 by Sanders et al. 1988; NGC 2623 by Bryant & Scoville 1999; and NGC 7252 by Wang, Schweizer, & Scoville 1992). These systems span the entire range of the sequence from beginning to end. We chose to improve our understanding of the dynamical effects occurring during merging encounters by observing additional systems at the beginning and end of the sequence (NGC 4676 and NGC 3921, respectively) and by reobserving NGC 520. We selected these three systems because there are VLA H I mapping and deep broadband and narrowband optical observations available to help in the interpretation of the CO data (from Hibbard & van Gorkom 1996, hereafter HvG96). We chose to reobserve NGC 520 to target explicitly the second nucleus, which did not fall within the previously observed field (Sanders et al. 1988). Previous observations and a detailed description of the three systems are found in HvG96. Here we summarize their defining optical morphological features and their location along the Toomre sequence. Excellent photographs of the systems can be found in the Arp "Atlas of Peculiar Galaxies" (Arp 1966), and CCD images of the entire systems, including the extended tidal features, are given in HvG96. In this paper, we will restrict our figures to the inner few kiloparsecs of each merger, as this is where the CO is concentrated.

NGC 4676 ("The Mice" = UGC 7938/39 = Arp 242 = VV 224) is the second member of the Toomre sequence, representing an early-stage merger in which the two disks are separated by less than 1 optical diameter in projection but still distinct. A bright optical bridge connects the two disks, and two distinct bright optical tails, each about 50 kpc in projected length,[2] are present.

NGC 520 (UGC 966 = Arp 157 = VV231) falls near the middle of the Toomre sequence (seventh of 11), representing an intermediate stage of merging in which two distinct nuclei are seen embedded within a single stellar body. The primary nucleus is hidden beneath the prominent dust lane near the remnant body center, and the secondary nucleus is seen 40″ (6 kpc) away toward the northwest. A bright optical tail stretches 25 kpc to the south, and a broad stellar plume is seen reaching 60 kpc to the northwest.

NGC 3921 (UGC 6823 = Arp 224 = Mrk 430) is the next to last member of the Toomre sequence. It represents the latest stages of a merger, with a single stellar remnant body exhibiting an $r^{1/4}$ radial light profile, which is characteristic of normal ellipticals. The optical isophotes are not concentric (Schweizer 1996, hereafter S96), suggesting that the merger is not fully relaxed. A stellar tail stretches 65 kpc to the south, and a broad optical plume reaches 80 kpc to the northeast.

3. OBSERVATIONS

Aperture synthesis CO observations of NGC 520, NGC 3921, and NGC 4676 were carried out with the Owens Valley Millimeter Array between 1994 September and 1995 February. There are six 10.4 m diameter telescopes in the array, providing a field of view of about 1′ (FWHM) at 115 GHz. The telescopes are equipped with SIS receivers cooled to 4 K, and typical single-sideband system temperatures were between 300 and 500 K. Baselines of 15–200 m east-west and 15–220 m north-south were used, and the details of the observations, including the synthesized beams from naturally weighted data are summarized in Table 1. A digital correlator configured with 120 × 4 MHz channels (11.2 km s^{-1}) covered a total velocity range of 1340 km s^{-1}. Nearby quasars (see Table 1) were observed at 25 minute intervals to track the phase and short-term instrument gain. Uranus (T_B = 120 K), Neptune (T_B = 115 K), 3C 273, and 3C 454.3 were observed for the absolute flux calibra-

[2] All length, mass, and luminosity scales in the following are derived assuming a value of the Hubble constant of $H_0 = 75$ km s^{-1} Mpc^{-1}.

TABLE 1

SUMMARY OF OBSERVATIONS

Properties	NGC 520 N	NGC 520 S	NGC 3921	NGC 4676
Phase center:				
α (B1950)	$01^h21^m58^s.8$	$01^h21^m59^s.4$	$11^h48^m28^s.9$	$12^h43^m44^s.5$
δ (B1950)	+03°32′17″.0	+03°32′09″.0	+55°21′10″.0	+31°00′02″.0
Center velocity (km s^{-1})	2260	2260	5838	6600
Gain calibrator	0106+013	0106+013	1150+497	1308+326
Flux calibrator	Uranus, Neptune, 3C 273, 3C 454.3			
Observed dates	1994 Sep 28, 1994 Oct 3, 1994 Dec 6, 1995 Jan 26, 1995 Feb 4		1994 Oct 21, 1995 Feb 13, 1995 Feb 20	1994 Oct 11, 1994 Dec 5, 1995 Jan 12
On-source integration (hr)	11.8	11.8	19.2	16.3
Sensitivity (mJy beam^{-1})	12.9[a]	12.9[a]	5.8[b]	8.1[b]
θ (FWHM) (P.A.)	2″.4 × 2″.7 (−83°)		2″.3 × 2″.7 (83°)	2″.8 × 3″.2 (87°)

[a] As measured in each of the 8 MHz (20.8 km s^{-1}) channel maps.

[b] As measured in each of the 16 MHz (41.6 km s^{-1}) channel maps.

tion. The data were calibrated using the standard Owens-Valley array program MMA (Scoville et al. 1993) and were mapped and analyzed using the imaging program DIFMAP (Shepherd, Pearson, & Taylor 1994) and the NRAO AIPS software system. The uncertainty in absolute flux calibration is about 15%, mainly because of the uncertainty in transferring the calibration between the sources and the flux calibrators.[3] The positional accuracy of the resulting maps is better than $\sim 0\farcs5$.

A detailed study of all three systems has been conducted in the optical and 21 cm H I emission by HvG96: radio synthesis observations of 21 cm H I emission to obtain information on the distribution and kinematics of extended cold atomic gas; deep broadband R images to delineate the underlying stellar distribution and any faint optical tidal extensions; and narrowband Hα + [N II] observations to reveal regions of current star formation. These data are compared with the CO distribution and kinematics in the present work and are fully described in HvG96.

Additional optical and near-infrared (NIR) data on NGC 3921 were needed to examine the dynamical state of this puzzling merger remnant. Broadband BVR observations of NGC 3921 were obtained in January of 1997 with the University of Hawaii 88 inch (2.2 m) (UH88) telescope. The f/10 reimaging optics were used with a Tek2048 CCD, resulting in a plate scale of $0\farcs22$ pixel^{-1} and a field of view of $7\farcm5$. The seeing was $\sim 1\farcs2$, and total exposure times of 1200, 900, and 600 s were obtained in B, V, and R, respectively. The data were calibrated via observations of Landolt (1983, 1992) standards observed on the same nights, with resulting zero-point errors (1 σ) of 0.01, 0.02, and 0.03 mag in B, V, and R.

NIR observations were made at K' band ($\lambda = 2.11$ μm, hereafter referred to simply as K; Wainscoat & Cowie 1992), obtained with the QUIRC 1024 × 1024 detector on the UH88 telescope in January of 1995. The f/10 reimaging optics were used, resulting in a plate scale of $0\farcs187$ pixel^{-1} and a field of view of $3\farcm2$. The observations consist of three 120 s target-sky pairs, with the CCD dithered by $1\farcm5$ between on-source positions. The NIR data are uncalibrated.

4. RESULTS

The observed and derived properties of the sample are summarized in Table 2 along with other properties of interest. The far-infrared (FIR) luminosities,[4] $L_{\rm FIR}$, of these three merging systems range between 1×10^{10} and 5×10^{10} $L_\odot$, with an $L_{\rm FIR}/L_B$ ratio of unity for NGC 4676 and NGC 520 and about 0.2 for NGC 3921. Therefore these are modest

[3] Relative accuracy among the measurements presented here is significantly better, but the absolute uncertainty is offered because it is more relevant when comparing these measurements with other measurements.

[4] $L_{\rm FIR}$ represents the IR luminosity in the 40–120 μm band, calculated from the 60 and 100 μm *IRAS* fluxes (see Helou et al. 1988).

TABLE 2

SUMMARY OF OBSERVED AND DERIVED PROPERTIES

Properties	NGC 4676A	NGC 4676B	NGC 520	NGC 3921
R. A. (B1950)	$12^{\rm h}43^{\rm m}44\fs1$	$12^{\rm h}43^{\rm m}45\fs3$	$01^{\rm h}21^{\rm m}59\fs6$	$11^{\rm h}48^{\rm m}28\fs9$
Decl. (B1950)	$+31°00'19''$	$+30°59'47''$	$+03°31'53''$	$+55^{\rm h}21'23''$
Distance (Mpc)[a]	88	88	30	78
$\langle V_{\rm CO,hel}\rangle$ (km s^{-1})	6632 ± 42	6590 ± 42	2247 ± 21	5880 ± 42
$\Delta V_{\rm CO,FWZI}$ (km s^{-1})	546 ± 42	252 ± 42	499 ± 21	462 ± 42
Deconvolution size (P.A.)	$8\farcs5 \times 1\farcs1$ (5°)	$16'' \times 2''$ (22°)	$7\farcs1 \times 2\farcs9$ (95°)	$5\farcs0 \times 2\farcs3$ (38°)
	(3.6 × 0.5 kpc)	(7 × <1 kpc)	(1.0 × 0.4 kpc)	(1.9 × 0.9 kpc)
$\Delta T_{\rm CO,\ peak}$ (K)	0.60 ± 0.09	0.28 ± 0.04	5.2 ± 0.7	0.64 ± 0.09
$S_{\rm CO}\Delta V$ (Jy km s^{-1}):				
OVRO	54 ± 8	14 ± 2	404 ± 61	25 ± 4
Single-dish[b]	55	34	696	21
$M_{\rm H_2,\ OVRO}$ ($M_\odot$)[c]	$(4.9 \pm 0.7) \times 10^9$	$(1.3 \pm 0.2) \times 10^9$	$(4.3 \pm 0.7) \times 10^9$	$(1.8 \pm 0.3) \times 10^9$
$N_{\rm H_2,\ peak}$ (cm^{-2})	$(6.1 \pm 0.9) \times 10^{22}$	$(1.6 \pm 0.0.2) \times 10^{22}$	$(3.0 \pm 0.5) \times 10^{23}$	$(3.7 \pm 0.6) \times 10^{22}$
$\Sigma_{\rm H_2}$ ($M_\odot$ pc^{-2}):[d]				
Peak	900 ± 135	210 ± 32	4670 ± 700	540 ± 270
Mean	340 ± 51	24 ± 4	2650 ± 400	134 ± 20
$S_{1.4\ \rm GHz}$ (mJy)[e]	23.6	6.6	158	9.4
$\log L_{1.4\ \rm GHz}$ (W Hz^{-1})	22.0	21.4	21.9	21.5
IRAS 12 μm (Jy)[f]	(0.09 ± 0.03)		0.77 ± 0.06	0.12 ± 0.02
IRAS 25 μm (Jy)[f]	(0.48 ± 0.03)		2.87 ± 0.17	0.28 ± 0.02
IRAS 60 μm (Jy)[f]	(2.93 ± 0.04)		30.9 ± 1.9	0.83 ± 0.03
IRAS 100 μm (Jy)[f]	(5.26 ± 0.12)		45.8 ± 2.7	1.60 ± 0.11
$T_{\rm dust}$ (K)[g]	38		42	37
$L_{\rm FIR}$ ($L_\odot$)[g]	2.8×10^{10}	0.8×10^{10}	5.4×10^{10}	0.8×10^{10}
L_B (10^{10} $L_\odot$)[e]	2.8×10^{10}	1.6×10^{10}	3.4×10^{10}	5.5×10^{10}

[a] $H_0 = 75$ km s^{-1} Mpc^{-1} assumed.

[b] Single-dish references: NGC 4676, Casoli et al. 1991; NGC 520, Young et al. 1995; NGC 3921, F. Combes 2000, private communication.

[c] $M_{\rm H_2} = 1.2 \times 10^4 S_{\rm CO}\Delta V D^2_{\rm Mpc}$ $M_\odot$ (see Sanders, Scoville, & Soifer 1991).

[d] $\Sigma_{\rm H_2} = M_{\rm H_2} \times [\pi R^2/ln2]^{-1}$.

[e] From HvG96.

[f] From *IRAS* ADDSCAN/SCANPI (see Helou et al. 1988).

[g] $L_{\rm FIR} = 4 \times 10^5 (2.58 S_{60\mu\rm m} + S_{100\mu\rm m}) D^2_{\rm Mpc}$ $L_\odot$ and assuming dust emissivity $n = 1$ (see Helou et al. 1988). NGC 4676A and 4676B are not resolved by *IRAS*, and the FIR fluxes are estimated by the ratio of their 1.4 GHz radio continuum flux ratio.

starburst systems at best. The molecular gas masses[5] detected in CO range between 1×10^9 and 5×10^9 $M_\odot$, accounting for 40% to 100% of the gas masses inferred from single-dish measurements. This is within a factor of 2 of the *total* molecular gas associated with our Galaxy (3.5×10^9 $M_\odot$; Sanders, Solomon, & Scoville 1984). While the bulk of the molecular gas in our Galaxy is located within an annulus of 4–6 kpc radius, CO emission in these optically selected merger systems is concentrated in the central 2 kpc radius, except for NGC 4676B, the total molecular gas content and distribution of which are not well determined by our data (see below).

The CO (1–0) spectra of each system are produced by summing the detected emission from each narrowband channel map and are shown in Figure 1. All of the CO (1–0) spectra show line widths and shapes comparable to the single-dish spectra (*dotted lines*; Casoli et al. 1991; Solomon, Downes, & Radford 1992; F. Combes 2000, private communication). We do not recover the full line flux measured in the single-dish observations in some cases (see Table 2). Since the interferometer lacks spacings shorter than about 10 m, one possibility is that there is some extended CO emission ($\theta > 45''$) that is resolved out in our observations. Another possibility is that some of the line emission is lost to the limiting surface brightness sensitivity of the observations. The peak CO line brightness temperature observed is only about 0.3–0.6 K for NGC 3921 and NGC 4676 and 5.2 K for NGC 520. Since the intrinsic CO line brightness should be at least 10–20 K and may be as high as 30–50 K in starburst regions, the beam filling factor for the CO emitting regions must be quite small, less than 10% and significantly so in some cases.

The molecular gas distribution and kinematics in the individual systems are discussed in detail below. For all three observed mergers, we first compare the CO distribution with the *R*-band, narrowband Hα + [N II], and VLA H I distributions from HvG96. We then examine the full CO three-dimensional kinematic information as traced by the individual channel maps. From these plots, it is clear that the CO emitting molecular complexes are well resolved spatially and kinematically by the aperture synthesis observations presented here. We explore the CO kinematics by comparing the mean velocity and velocity dispersion maps. The mean velocity field gives an idea of the large-scale orbital motions, and the intensity-weighted velocity dispersion helps identify the local centers of the gravitational potential or the sites of large peculiar velocities. Finally, we plot the kinematic profiles along the major axis and compare these with the 21 cm line data and any available optical kinematics.

4.1. *NGC 4676*

4.1.1. *Molecular Gas Distribution*

We mapped the CO (1–0) emission in NGC 4676 ($D = 88$ Mpc) at $2''.8 \times 3''.2$ (1.2 × 1.4 kpc) resolution. The array was pointed at the region between the two nuclei such that the

[5] Standard Galactic conversion of $N_{H_2}/I_{CO} = 3 \times 10^{20}$ cm^{-2} (K km s^{-1})$^{-1}$ is used (see Young & Scoville 1991).

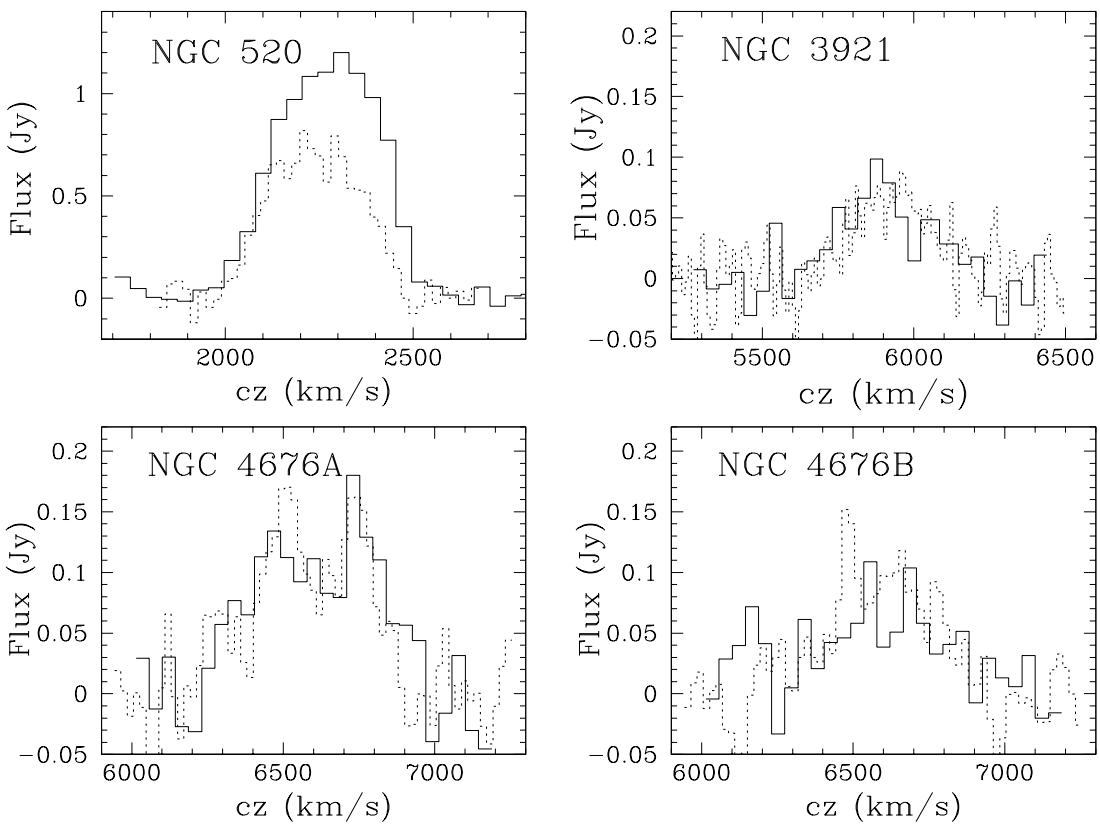

FIG. 1.—CO (1–0) spectra of the Toomre sequence mergers imaged. They are obtained by summing all detected fluxes in the individual channel maps (see Figs. 3, 7, and 14). Single-dish spectra from the IRAM 30 m telescope ($\theta_{FWHM} = 22''$) are shown in dotted lines (NGC 520 [Solomon et al. 1992], NGC 3921 [F. Combes 2000, private communication], NGC 4676 [Casoli et al. 1991]). The shape and the flux levels agree well between our measurements and the IRAM 30 m measurements, except in NGC 520 where the IRAM 30 m spectrum is significantly lower, possibly because of a pointing or calibration problem.

primary beam (field of view) of the array includes the main bodies of both galaxies but very little of the tidal tails (see Fig. 2, *left*). Both NGC 4676A (north) and NGC 4676B (south) are detected in emission, and the integrated CO emission is contoured in Figure 2. About 80% of the CO emission is associated with NGC 4676A, while only weak CO emission is detected along the bar in NGC 4676B. The total detected CO flux in NGC 4676A is 54 ± 8 Jy km s^{-1} (100% of the flux measured by the IRAM 30 m telescope by Casoli et al. 1991), which corresponds to a total molecular gas mass of $5.5 \times 10^9\ M_\odot$ or about twice as much as in our Galaxy. In NGC 4676B, we recover only 20% of the total single-dish CO flux reported by Casoli et al. Our brightness sensitivity ($\Delta T_B = 0.08$ K) and a low beam filling factor may explain at least part of the "missing" flux. When the visibility data are tapered to $\sim 5''$ resolution, the recovered flux increased to 14 ± 2 Jy km s^{-1}, or about 40% of the total single-dish flux. The CO morphology does not change substantially in the low-resolution maps, however. The undetected single-dish flux is associated with a distinct spiky spectral feature occurring between the velocities of 6400 and 6800 km s^{-1} in Figure 1. This feature may arise from the molecular gas associated with the bridging region, which is poorly represented in our data owing to a low beam filling factor. Alternatively, this feature may be CO emission from NGC 4676A picked up by the sidelobe response of the IRAM 30 m telescope rather than being intrinsic to NGC 4676B.

The CO emission in NGC 4676A is clearly confined to a nearly edge-on disklike structure with a deconvolved size of 1.8 kpc in radius and a thickness (FWHM) of 250 pc (see Table 2). A bridge of stars and gas connecting the two galaxies is clearly seen in the optical and H I emission (see Fig. 2, *right*), and several CO clumps are also found in the bridging region (i.e., at velocities between 6641 and 6558 km s^{-1} in Fig. 3), albeit with relatively low signal-to-noise ratio (S/N). Only one such CO clump appears in the velocity-integrated CO map (Figs. 2, *left*, and 4*a*), just southeast of the main body of NGC 4676A, because only the high-S/N ($\geq 5\ \sigma$) features are included in these maps. The presence of molecular gas in the bridging region suggests that the disruption of the inner disks ($R < 10$ kpc) has begun in NGC 4676. Most of the CO clumps seen in the channel map are unresolved ($\lesssim 1$ kpc in diameter), with molecular gas masses of $\sim 10^8\ M_\odot$. They are somewhat larger and more massive than the giant molecular clouds (GMCs) in our Galaxy, and they may be responding ballistically to the tidal disruption. Alternatively, these CO clumps may be molecular gas condensations forming within the gaseous bridge traced in H I and may represent possible sites of future star formation.

One striking feature in the distribution of CO emission in NGC 4676 is the lack of any correspondence between the brighter Hα peaks (presumably tracing the present sites of star formation) and the CO peaks (dense gas concentrations). Even a marginal anticorrelation is seen, particularly in Figure 4*a*, which displays a wider intensity scale for the Hα emission than shown in Figure 2 (*middle*). The brightest Hα emission in NGC 4676A is located just outside the southern tip of the CO emitting region, and significant optical extinction in this nearly edge-on disk offers a natural explanation—the peak integrated CO flux of 18 ± 3 Jy km s^{-1} beam^{-1} corresponds to $N_{\rm H_2} = 6.1 \times 10^{22}$ cm^{-2} and a mean visual extinction of $A_V \sim 120$ averaged over the $3''$ (1.3 kpc) beam. Even the lowest CO contour in Figure 4*a* corresponds to $A_V \sim 12$.

For the more face-on galaxy NGC 4676B, CO and Hα emission do not correspond well either. The brightest Hα peak near the center of the galaxy has no associated CO emission, and this may indicate that the lifetime for young stars may be much longer than the cloud dispersion time-

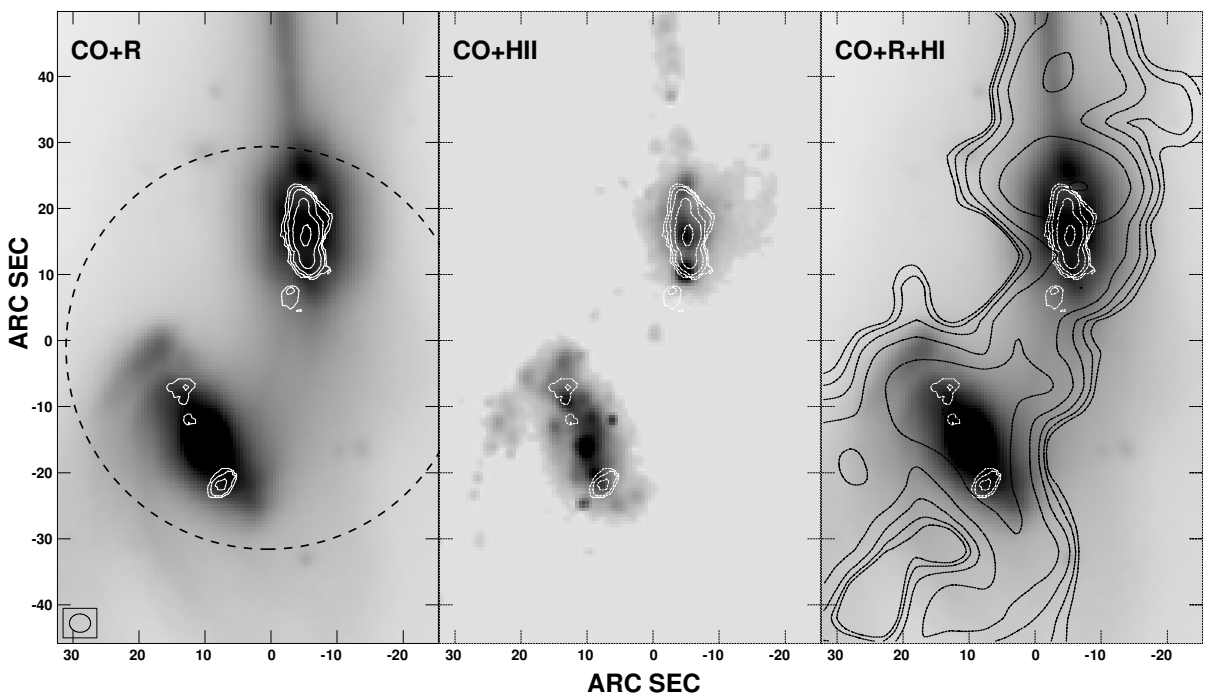

FIG. 2.—Velocity-integrated CO (1–0) map of NGC 4676 at $2''.8 \times 3''.2$ (1.2×1.4 kpc, P.A. = 87°) resolution superposed over the *R*-band image (*left*), Hα (*middle*), and 21 cm H I (*right*) for comparison. An angular separation of $20''$ corresponds to 8.5 kpc at the assumed distance of 88 Mpc. The field of view of the OVRO dishes at 115 GHz (1′ FWHM) is indicated by a dashed circle. The CO contours (*white*) are drawn at levels of 50, 100, 200, 400, and $800\ M_\odot$ pc^{-2}, and the H I contours correspond to column densities of 5, 10, 20, 40, and 80 times 1×10^{19} cm^{-2}.

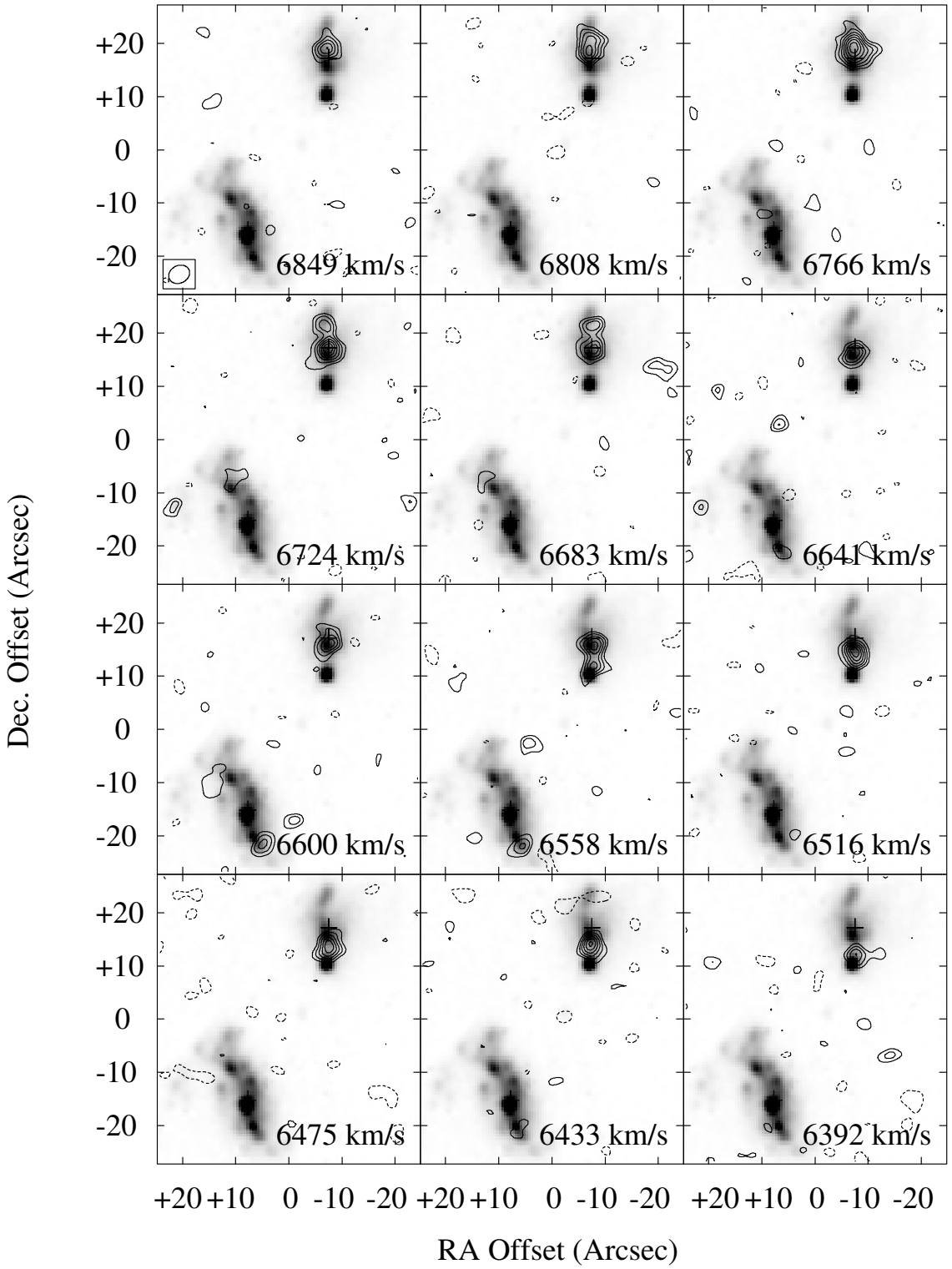

FIG. 3.—Individual channel maps of CO (1–0) emission in NGC 4676 with 2.″8 × 3.″2 (1.2 × 1.4 kpc, P.A. = 87°) resolution, shown in 41.6 km s^{-1} velocity increments on a gray-scale representation of the Hα image. The brightest peak (79.2 mJy beam^{-1}) corresponds to a brightness temperature of 0.60 K above the microwave background. The contour levels are −2, +2, +3, +4, +5, +6, +7, and +8 times 9 mJy beam^{-1} (1 σ). The dominant CO source is NGC 4676A, and some CO clumps are also seen in NGC 4676B. Several spatially and kinematically coherent CO features in the region bridging the two galaxies (V = 6516 to 6641 km s^{-1}) suggest the presence of molecular gas in this overlap region.

scale. The observed "twin-peak" CO morphology is often seen in other barred galaxies, probably caused by a bar-driven dynamical resonance within these disks (Kenney et al. 1992). Figure 2 (*middle*) shows that both the CO and Hα bars are offset in the same manner from the underlying optical bar (HvG96). Similar offsets are seen in hydrodynamic simulations of mergers (Barnes & Hernquist 1991) and provide a means of transferring angular momentum from the gas to the stars, allowing the gas to settle even deeper into the potential.

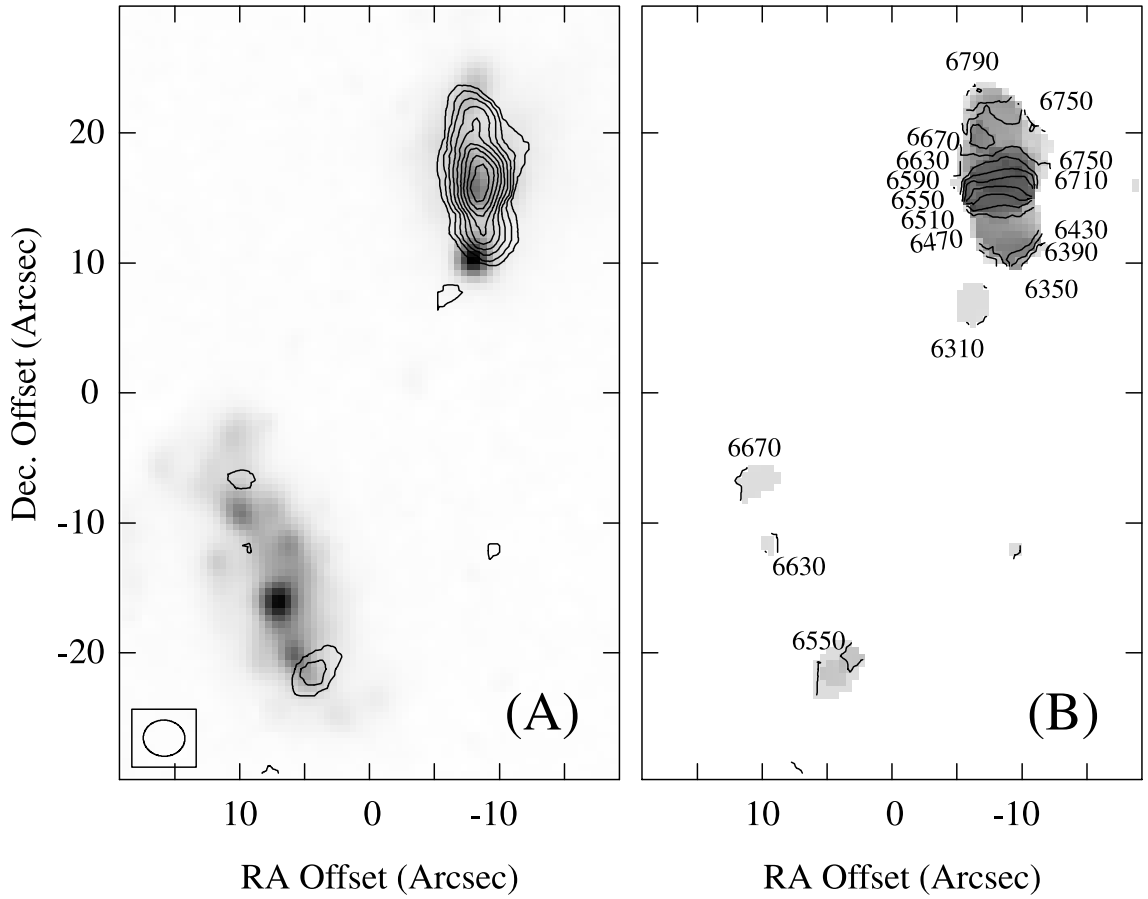

FIG. 4.—(*a*) Velocity-integrated CO (1–0) map of NGC 4676 in linear contours superposed over the Hα image. The contours are 10, 20, 30, 40, 50, 60, 70, 80, and 90 percent of the peak, which is 18.4 Jy km s^{-1} ($N_{H_2} = 6.1 \times 10^{22}$ cm^{-2}). Only weak CO emission is detected along the bar in NGC 4676B. The spatial correspondence between the CO and Hα is poor, and extinction by dust associated with the molecular gas (peak $A_V \sim 120$) offers a natural explanation in the edge-on system NGC 4676A. (*b*) Mean CO emission velocity plotted in contours (in km s^{-1}) superposed over the velocity dispersion ("second moment") map in gray scale. The linear gray-scale range is between 0 (*white*) and 160 km s^{-1} (*black*). The velocity gradient is increasing to the north in both galaxies, and thus the spin orientation of the collision is in a prograde sense.

Another notable aspect of the CO emission in NGC 4676 is the apparent contrast in CO luminosity and distribution between the two merging galaxies. We detect about 4 times more CO emission in NGC 4676A with a much more centrally concentrated distribution compared with that of NGC 4676B. The apparent contrast in the CO luminosity in the single-dish measurements by Casoli et al. (1991) is about a factor of 2, and some of the CO emission associated with NGC 4676B may extend beyond the inner disk region mapped by us (see above). One explanation for the apparent difference in the gas content is that the progenitor disk for NGC 4676B had less molecular gas. The two merging galaxies have similar total H I content (about 3×10^9 $M_\odot$ each; HvG96), but NGC 4676B appears to be an earlier Hubble type (SB0/a). In a survey of molecular gas content among S0 and Sa galaxies, Thronson et al. (1989) conclude that typical fractional gas masses in S0's and Sa's are about an order of magnitude less than those for Sb or Sc spirals, and Young & Knezek (1989) report the largest $M(H_2)/M(\text{H I})$ ratios among the S0/Sa Hubble types.[6] Alternatively, the two progenitor disks started off with similar amounts of molecular gas but evolved differently under the tidal disruption because of different internal structure or different spin-orbit alignment (see Mihos & Hernquist 1996). The difference between these two scenarios has important consequences for understanding how a gas disk responds to a tidal disruption. Our observations alone cannot distinguish the two, however, and this issue needs to be addressed by future numerical studies.

[6] However, the scatter associated with the individual Hubble type is substantial in both studies.

4.1.2. *Molecular Gas Kinematics*

NGC 4676A shows a distinct and relatively intact molecular gas distribution with relatively undisturbed kinematics. The intensity-weighted mean CO velocity is shown in contours superposed over the gray-scale velocity dispersion ("second moment") map in Figure 4*b*. The velocity dispersion shown in Figure 4*b* exhibits a distinct peak at the center of NGC 4676A. This arises from the rapid rise in the CO rotation curve and therefore marks the dynamical center of this edge-on disk. The major-axis position-velocity plot (Fig. 5) shows more clearly that the CO emitting molecular gas in NGC 4676A is in rotation about its center, and an apparent flattening of the rotation curve is hinted at by the sudden drop in the velocity gradient outside the central 4″–5″ (2 kpc) region. The line-of-sight velocity for the CO emission sharply decreases at 2″.5 (1.1 kpc) radius, forming an S-shaped feature in the position-velocity plot. As shown by the solid lines in Figure 5, the H I rotation curve remains flat, and this CO kinematic signature probably does not

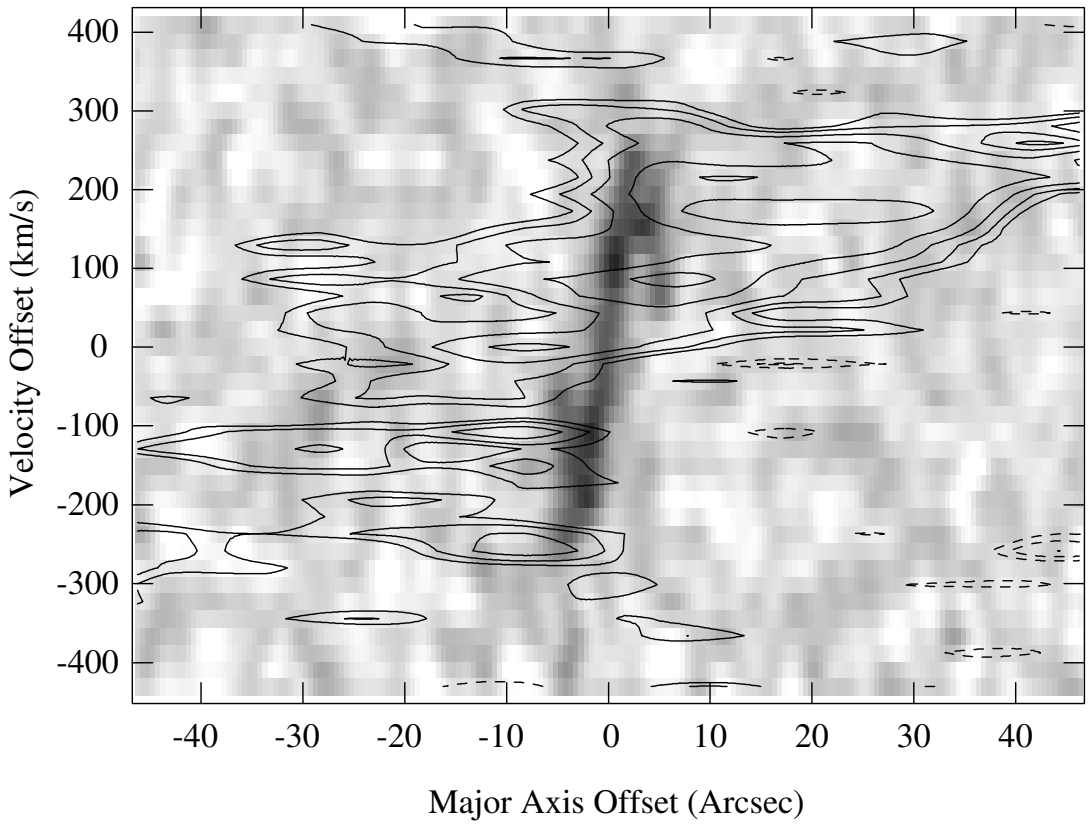

FIG. 5.—Position-velocity plot of CO emission in NGC 4676A along the kinematic (and morphological) major axis shown in gray scale. Molecular gas traces the kinematics of the inner disk with a rising rotation curve with a maximum rotation velocity of 270 km s^{-1}, which flattens at a radius of 960 pc. Contours represent the corresponding *P-V* plot of the 21 cm H I emission (from HvG96), which is a good indicator of the extent of the outer disk with a flat rotation curve. They both suggest that the kinematics of the inner gas disk ($R < 4$ kpc) is relatively undisturbed. The S-shaped morphology of the CO emission indicates that the molecular gas does not uniformly fill the disk outside 1 kpc radius and may be confined to a pair of tightly wound spiral arms.

indicate a real drop in rotation velocity and may arise from noncircular motions induced by a nonaxisymmetric potential. A pair of tightly wound molecular spiral arms can also exhibit a similar kinematic signature.

The peak rotation velocities traced in CO, H I, and Hα are all about 270 km s^{-1}. The large aspect ratio of the CO emitting region suggests that the molecular gas disk is viewed within 5°–10° of being edge-on, and the observed peak rotation velocity should be a good estimate for the true disk rotation speed. The derived dynamical mass,[7] $M_{\rm dyn} = V^2R/G$, inside the 1.8 kpc radius is then 2.9×10^{10} $M_\odot$, and the molecular gas mass inferred from the CO emission (4.9×10^9 $M_\odot$) accounts for about 20% of this dynamical mass. This gas mass fraction is on the upper end of what is seen in ordinary disk galaxies (a few to 25%; see Young & Scoville 1991 and references therein).

The orbital motion of the molecular gas in NGC 4676B is more difficult to determine because of its more face-on projection and the patchy CO distribution. The observed CO kinematics is consistent with the Hα rotation curve derived by Mihos et al. (1993) along the bar, which shows a monotonic velocity gradient consistent with solid-body rotation. Assuming a disk inclination of 45°, the dynamical mass inside the 4 kpc radius is about 2×10^{10} $M_\odot$. The derived molecular gas mass fraction is then about 7%, which is more typical of undisturbed disk galaxies.

The systemic velocities of the two galaxies are very similar (NGC 4676A slightly more redshifted, by ~60 km s^{-1}), suggesting that the two disks are either near their orbital apocenter or moving mostly in the plane of the sky. The velocity gradient increases to the north in both galaxies, consistent with the H I kinematics reported by HvG96 and the Hα kinematics measured by Stockton (1974) and Mihos et al. (1993). The spin vectors of the two disks are aligned with their orbital motion, and the large tidal tails emerging from both disks are naturally explained by this prograde spin-orbit resonance (Toomre & Toomre 1972). The CO emitting clouds seen in the bridging region between the two merging disks have velocities intermediate between the systemic velocities of the two disks as expected.

4.2. *NGC 520*

4.2.1. *Molecular Gas Distribution*

We mapped the CO (1–0) emission in NGC 520 ($D = 30$ Mpc) at 2.″3 × 2.″7 (0.34 × 0.41 kpc) resolution, which is a factor of 2 improvement over the previous OVRO CO map by Sanders et al. (1988; 6″ × 5″). Two separate fields were observed, one centered on each of the NIR nuclei (Stanford & Balcells 1990), but CO emission is detected only around the main nucleus (see Fig. 6). The 3 σ upper limit for the molecular gas mass within the 1.3 kpc diameter region surrounding the second nucleus is 5×10^6 $M_\odot$, assuming a total line width of 60 km s^{-1}. This is less than 0.3% of the

[7] The dynamical mass estimate depends on the assumed mass distribution, and a simple rotational support approximation may result in a slight overestimation if the mass distribution is disklike rather than halo-like (see Binney & Tremaine 1987).

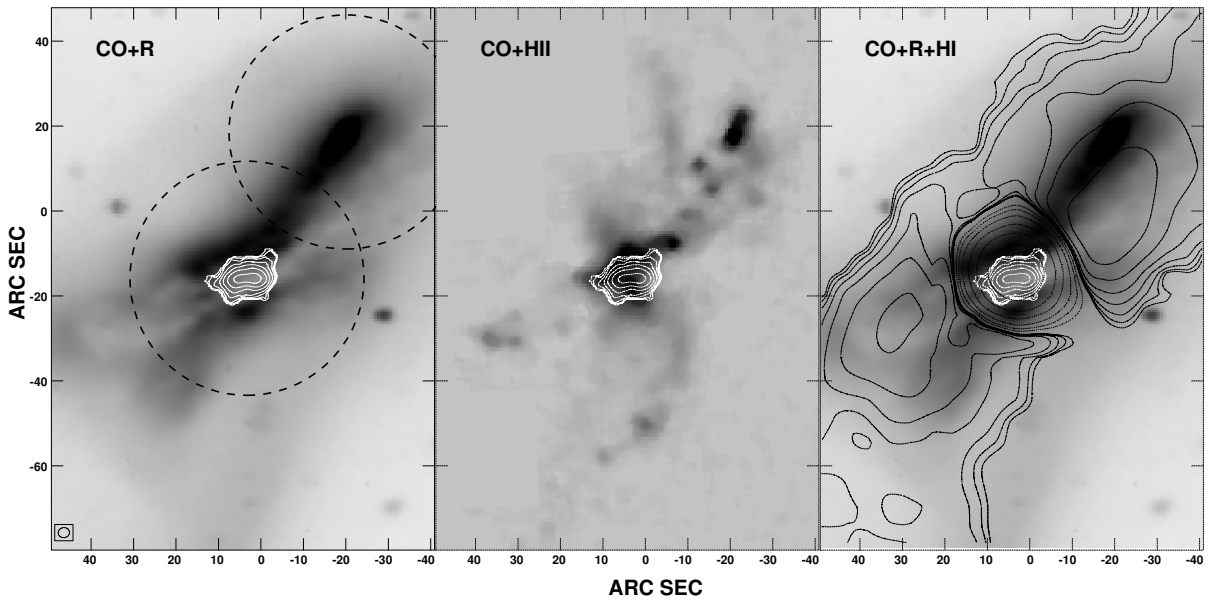

FIG. 6.—(*a*)–(*c*): Velocity-integrated CO (1–0) map of NGC 520 at 2″.4 × 2″.7 (0.34 × 0.41 kpc, P.A. = −83°) resolution superposed over the *R*-band image (*left*), Hα (*middle*), and 21 cm H I (*right*) for comparison. The location and FOV of the two pointings are indicated by the dashed circles. The CO emission is not aligned with the large-scale structure of the optical galaxy, which may be the result of accretion of material with angular momentum not aligned with the stellar disk. The CO contours (*white*) are drawn at levels of 50, 100, 200, 400, 800, 1600, and 3200 $M_\odot$ pc^{-2}. The H I contours correspond to column densities of 5, 10, 20, 40, 80, 160, and 320 times 1 × 10^{19} cm^{-2}, with dotted contours indicating H I absorption.

molecular gas mass associated with the main nucleus, and the contrast in the associated gas mass is quite dramatic. The absence of an associated molecular gas complex would be somewhat unusual if this were a true stellar nucleus of a late-type galaxy, and we will discuss this point further below (see § 5).

Nearly all of the 3.0 × 10^9 $M_\odot$ of molecular gas detected in the main nucleus position is concentrated in the 1.0 × 0.4 kpc (P.A. = 95°) disk mapped by Sanders et al. (1988), coincident with the bright, extended nuclear radio source (Condon et al. 1990). The mean H_2 density is about 10^3 cm^{-3} if the molecular gas is uniformly distributed in a disk with 500 pc radius and 100 pc thickness, as if the entire molecular complex were a single supermassive GMC. The full-resolution data result in a detected flux of 285 ± 43 Jy km s^{-1}, which is less than the 325 Jy km s^{-1} detected by Sanders et al. (1988). Smoothing the data to the 6″ resolution of Sanders et al. recovers a total flux of 404 ± 61 Jy km s^{-1}. The lower resolution maps do not reveal any additional features in the CO maps. Our measured flux corresponds to 58% of the total CO flux measured by the 14 m FCRAO telescope in its central 45″ beam area (Young et al. 1995). Solomon et al. (1992) report a total integrated line flux of only 211 Jy km s^{-1} within the 22″ beam of the IRAM 30 m telescope. Therefore it is likely that we recovered most of the flux associated with the nuclear molecular disk, but there may also be significant systematic errors associated with all of these line-flux measurements.

The partial mapping of CO emission by Young et al. suggests that CO emission extends beyond the nuclear region, along the stellar body of the galaxy (P.A. ∼ 45°). This extended CO emission is not detected, either because it is resolved out by the interferometer or because it has insufficient filling factor to be detected by the brightness limit of the synthesized beam (ΔT_B = 0.18 K). Evidence for some extended, diffuse gas is seen in the channel maps (Fig. 7, especially channels at 2195 and 2153 km s^{-1}), and its position angle with respect to the nuclear disk suggests that the extended gas may be associated with either the large-scale H I disk or with the gas entrained in a galactic superwind emerging along the minor axis (HvG96).

The anticorrelation between Hα and CO emission is even more dramatic in the nuclear region of NGC 520. The clear displacement of the CO emission from the Hα distribution shown in Figure 8*a* suggests that the Hα emission associated with the nuclear starburst is completely obscured by the dust within the nuclear gas disk. The peak integrated CO flux of 63.9 Jy km s^{-1} beam^{-1} corresponds to a mean column density of N_{H_2} = 3.0 × 10^{23} cm^{-2} averaged over the 2″.5 (375 pc) beam, and the inferred large optical extinction ($A_V \sim 600$) is entirely consistent with the complete obscuration of the nuclear starburst by the CO emitting clouds. The observed Hα emission is likely dominated by the starburst-driven ionized wind escaping along the poles and some scattered light from the nuclear starburst region. The 1.4 GHz radio continuum map of the nucleus of NGC 520 by Condon et al. (1990) is essentially identical in appearance and dimension (5″ × 2″, P.A. = 93°) and is coincident with the CO disk shown in Figure 8*a*. This is further strong evidence that the vigorous starburst activity is indeed associated with the molecular gas complex but entirely obscured. Similarly heavy obscuration of the starburst is found in other well-studied nuclear starburst systems such Arp 220 (Scoville, Yun, & Bryant 1997). The observed anticorrelation between CO and Hα not only confirms the diminished Hα emission from massive young stars by extinction (e.g., Bushouse et al. 1988; Kennicutt 1989; Cram et al. 1998), but it also casts a serious doubt on star formation rates inferred from optical or UV tracers for such starburst systems.

The appearance of the brightest CO emission at the most extreme velocities seen in the major-axis position-velocity plot (Fig. 9), as well as the flatness of the CO emission along the major axis in the velocity-integrated map (Fig. 8*a*), sug-

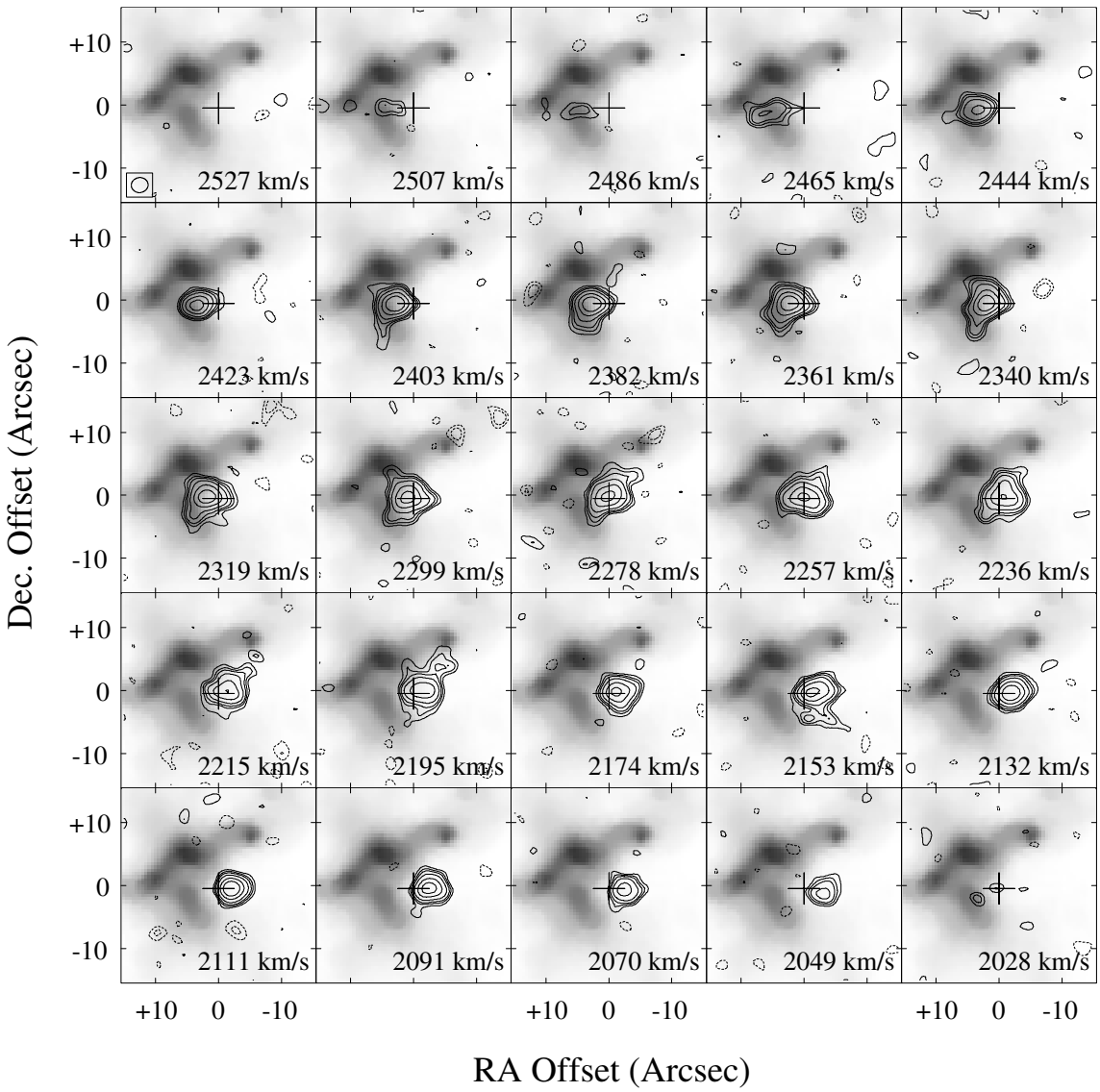

FIG. 7.—Individual channel maps of CO (1–0) emission in NGC 520 with 2.″4 × 2.″9 (0.34 × 0.41 kpc, P.A. = −83°) resolution shown in 20.8 km s^{-1} velocity increments contoured on the gray-scale representation of the Hα image. The plus sign marks the position of the bright radio continuum nucleus. The brightest peak (351 mJy beam^{-1}) corresponds to a brightness temperature of 5.2 K. The contour levels are −3, −2, +2, +3, +4, +6, +10, +15, and +25 times 15 mJy beam^{-1}. In addition to the clear rotation signature about the radio nucleus at P.A. = 0°, there is some evidence for gas associated with the large-scale tilted disk (P.A. = +45°) or perhaps gas associated with the nuclear blowout (see channels for V = 2153 and 2195 km s^{-1}).

gests that the CO emission does not rise monotonically inward but has a central hole, i.e., there is a nuclear molecular torus rather than a disk (contrast CO contours in Fig. 8*a* with those for NGC 4676A in Fig. 4*a*). This geometry has some similarity to the molecular torus found in the nuclear starburst region in M82 (Lo et al. 1987; Shen & Lo 1995), and such a central hole may be a common feature among nuclear starburst systems (e.g., Downes & Solomon 1998; Carilli, Wrobel, & Ulvestad 1998).

4.2.2. *Molecular Gas Kinematics*

The intensity-weighted mean CO velocity is shown in contours superposed over the gray-scale velocity dispersion map in Figure 8*b*. The CO emitting molecular gas in the nuclear region of NGC 520 shows a smooth, monotonic velocity gradient of 0.36 km s^{-1} pc^{-1}, which is a clear signature of rotation about its center. The regular interval of the isovelocity contours suggests a solid-body rotation, which is more evident in the major-axis position-velocity plot shown in Figure 9. The 21 cm H I absorption (*dashed contours* in Fig. 9) coincides with that of the CO emission, and this suggests the presence of neutral atomic gas intermixed with the molecular gas in the nuclear starburst region.

The CO line widths are represented by the gray-scale image in Figure 8*b*. The broadening of the line width toward the center of the CO complex suggests that the molecular gas is well centered on the galaxy nuclear potential. The channel maps and the isovelocity contours suggest that the molecular gas disk (or torus) is well resolved and is close to but not exactly edge-on. Assuming an intrinsic thickness of 100 pc, we infer an inclination of 70°–75° from the aspect ratio of the CO emitting region. The peak rotation velocity traced in CO is about 200 km s^{-1} (210 km s^{-1} correcting for i = 70°). Then the dynamical mass inside the 500 pc radius is 4.9 × 10^9 $M_\odot$, and the H_2 mass inferred from the CO emission (4.3 × 10^9 $M_\odot$, see Table 2) nearly entirely accounts for the total mass inside the 500 pc radius

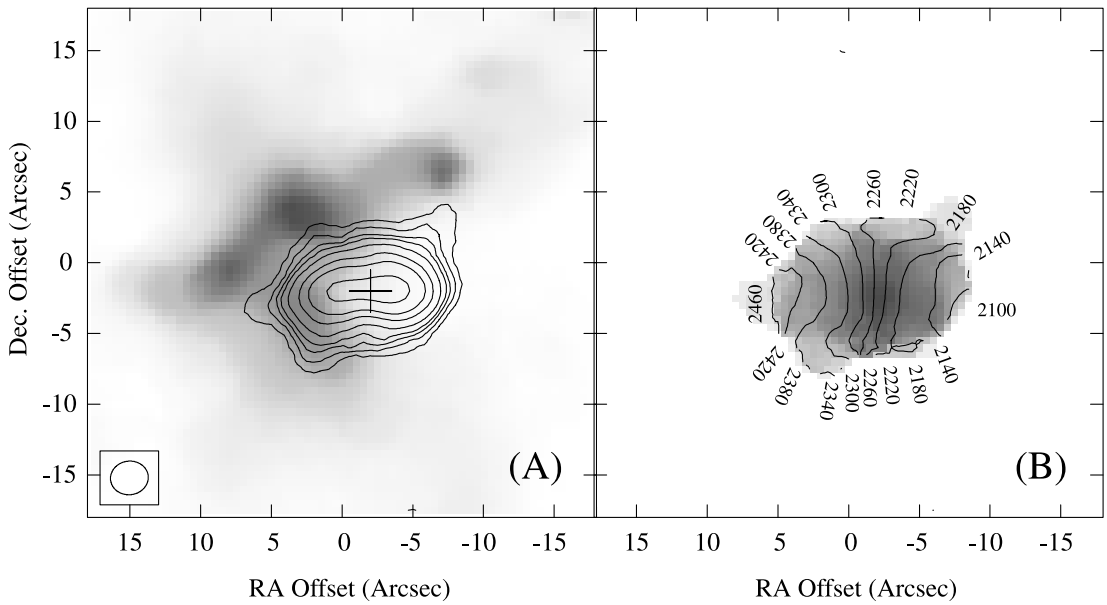

FIG. 8.—(*a*) Velocity-integrated CO (1–0) map of NGC 520 in contours superposed over the Hα image. The contour levels are 2, 4, 6, 8, 12, 20, 30, and 50 Jy km s^{-1}, and the peak integrated flux observed is 63.9 Jy km s^{-1}($N_{\mathrm{H_2}} = 3.0 \times 10^{23}$ cm^{-2}). Only the central 5 × 5 kpc region surrounding the primary nucleus of NGC 520 is shown since CO is not detected elsewhere. This integrated CO map has a remarkably similar appearance to that of the 1.4 GHz radio continuum map by Condon et al. (1990), while the Hα emission appears to avoid the CO emission. A larger Hα image (shown in Fig. 6) suggests that this ionized hydrogen emission is dominated by the bipolar wind blown out of the intense nuclear starburst region, and the starburst is completely obscured by the dust associated with the dusty torus mapped in CO (peak $A_V \sim 600$). (*b*) Mean CO emission velocity plotted in contours (in km s^{-1}) superposed over the velocity dispersion (" second moment ") map in gray scale. The linear gray-scale range is between 0 (*white*) and 120 km s^{-1} (*black*). The well-organized velocity field and centrally peaked velocity dispersion suggest that the molecular gas in NGC 520 is in rotation about the primary nucleus.

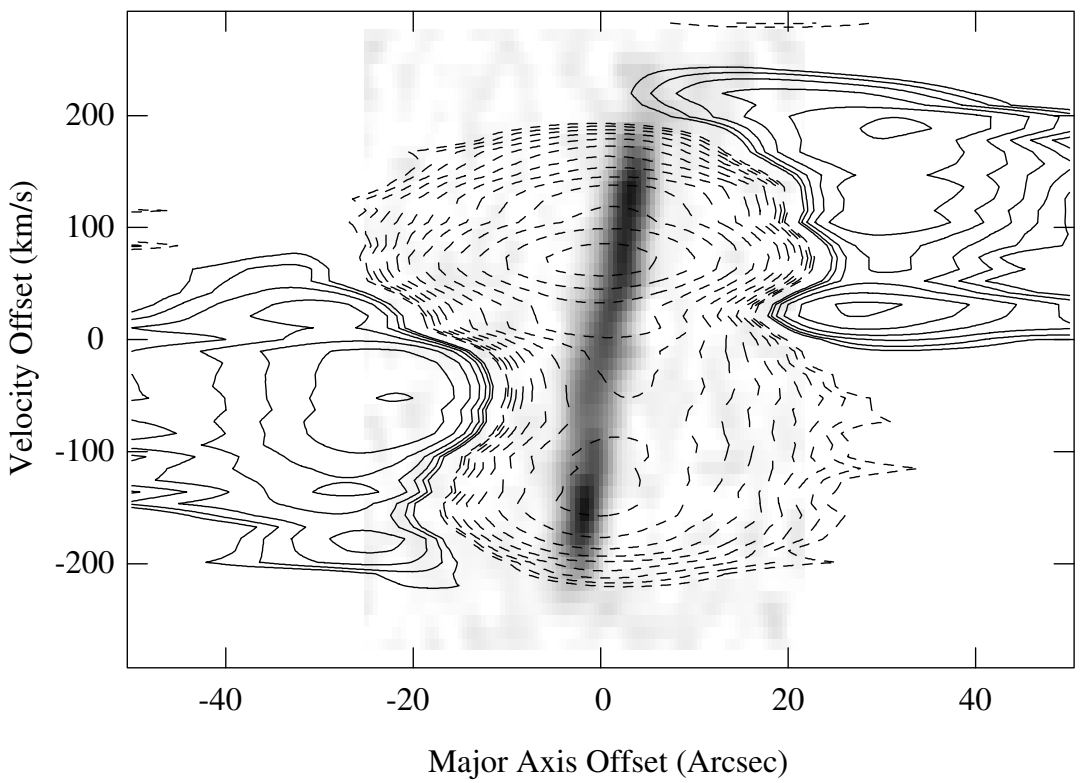

FIG. 9.—Position-velocity plot of CO emission in NGC 520 along the kinematic (and morphological) major axis shown in gray scale. The constant linear gradient suggests that the molecular disk in NGC 520 lies within the solid rotation part of the inner disk. The dark contours represent the corresponding *P-V* plot of 21 cm H I emission (dotted lines represent H I absorption—from HvG96), and the comparison with the CO emission suggests that the rotation curve turns over at the location of the outer radius of the molecular disk at a 500 pc radius with a maximum rotation speed of 200 km s^{-1}. The brightest CO emission occurs at both extreme velocities, suggesting that the CO emission decreases toward the center (see § 4.2.2).

region. This is a larger fraction than in NGC 4676A (§ 4.1.2) and is similarly dominant, as in the IR-luminous mergers such as Mrk 231 and Arp 220 (Bryant & Scoville 1996; Scoville et al. 1997). The higher density and temperature conditions associated with the intense starburst regions may result in an overestimation of molecular gas mass if the standard CO-to-H_2 conversion is used (Scoville et al. 1997; Downes & Solomon 1998), and the actual molecular gas mass traced by CO emission may be smaller by a factor of 2 or more. The orbital period at 500 pc radius is 2×10^7 yr, which is comparable to the timescale for the starburst but 2 orders of magnitude smaller than the dynamical timescale for the merger (HvG96).

One unusual aspect of the nuclear gas torus is that its position angle and angular momentum vector are misaligned with the larger scale stellar structures and outer H I disk. A similar misalignment of the nuclear disk is seen in other nuclear starburst systems, such as M82, and may be produced by accretion of inflowing gas with misaligned angular momentum. The observed behavior is probably transient in nature, as the continuing infall of mass and resulting torque will continue to shape the potential. The systemic velocity of the molecular gas disk, 2247 km s^{-1}, is in good agreement with that of the large-scale stellar and H I disks (Stockton & Bertola 1980; Stanford & Balcells 1990; HvG96).

4.3. *NGC 3921*

4.3.1. *Molecular Gas Distribution*

NGC 3921 ($D = 78$ Mpc) was detected previously in CO (1–0) and CO (2–1) emission with the IRAM 30 m telescope by Combes and collaborators (F. Combes 2000, private communication). We mapped the CO (1–0) emission in NGC 3921 at 2.″3 × 2.″7 (0.87 × 1.0 kpc) resolution, finding the emission confined to at least two separate complexes (see Fig. 14 below): a main complex of 2 kpc diameter near the center of the field and an unresolved CO emitting cloud located 7″ (2.6 kpc) south of the nucleus. The inferred molecular gas masses are 1.6×10^9 and 2.0×10^8 $M_\odot$, respectively. We recover all of the CO flux detected at the central position by the 22″ beam of the IRAM 30 m telescope (see Fig. 1 and Table 2), but the CO emission may extend beyond the area we mapped (F. Combes 2000, private communication). The mean H_2 density for the main molecular gas complex is ~ 150 cm^{-3} if the assumed line-of-sight thickness is 100 pc. This mean density is about one-sixth of that in NGC 520 but comparable to the typical density in Galactic GMCs.

The integrated CO emission map and the derived mean velocity field are shown in comparison with the H I and Hα emission in Figures 10 and 11. The locations of the optical, NIR, and radio continuum peak are coincident to within a fraction of an arcsecond, and the mean position is marked with a plus sign. The main molecular complex in NGC 3921, however, is displaced by about 2″ (∼ 760 pc) west of this location. This suggests either that the gas is physically displaced from the optical nucleus or that the true nucleus lies totally obscured beneath the CO complex (as is the case for NGC 520 and NGC 4676A).

These possibilities are further investigated by comparing the CO distribution with the optical and NIR (2.15 μm) images, as shown in Figure 12. The optical and NIR images are found to be coincident to within a fraction of a pixel (∼0.″2), while the peak of the CO emission is displaced by at least 10 pixels (2″) to the west. Further, the K-band image and $B-K$ color map show no hint of a hidden NIR peak beneath the CO complex. While the peak extinction inferred from our CO observation is large ($A_V \sim 70$, $A_K \sim 7$), evidence for a second nucleus would be visible in the NIR image if an extended stellar bulge were present. It therefore seems that the observed displacement between the molecular gas and the stellar nucleus is real. The CO emission appears to be associated with a concentration of dust, as indicated by the dark gray-scales in the $B-K$ map in Figure 12.

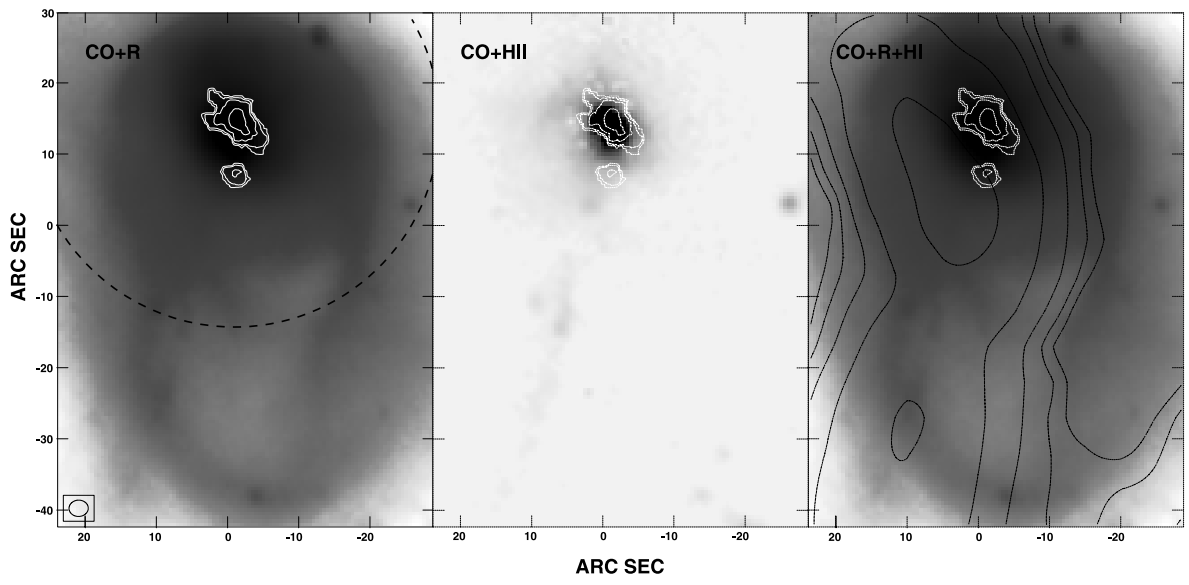

FIG. 10.—Velocity-integrated CO (1–0) map of NGC 3921 at 2.″3 × 2.″7 (0.87 × 1.0 kpc, P.A. = 83°) resolution superposed over the R-band image (*left*), Hα (*middle*), and 21 cm H I (*right*) for comparison. An angular separation of 20″ corresponds to 7.5 kpc at the assumed distance of 78 Mpc. The CO emission appears centered on the remnant on these angular scales (15″), but it is displaced from the brightest optical peak, as seen in the comparison with Hα and as in Fig. 11. The CO features occur near the ridge of bright H I emission, but they do not coincide with the H I peaks. The CO contours (*white*) are drawn at levels of 50, 100, 200, and 400 $M_\odot$ pc^{-2}, and the H I contours correspond to column densities of 5, 10, 20, 40, and 80 times 1×10^{19} cm^{-2}.

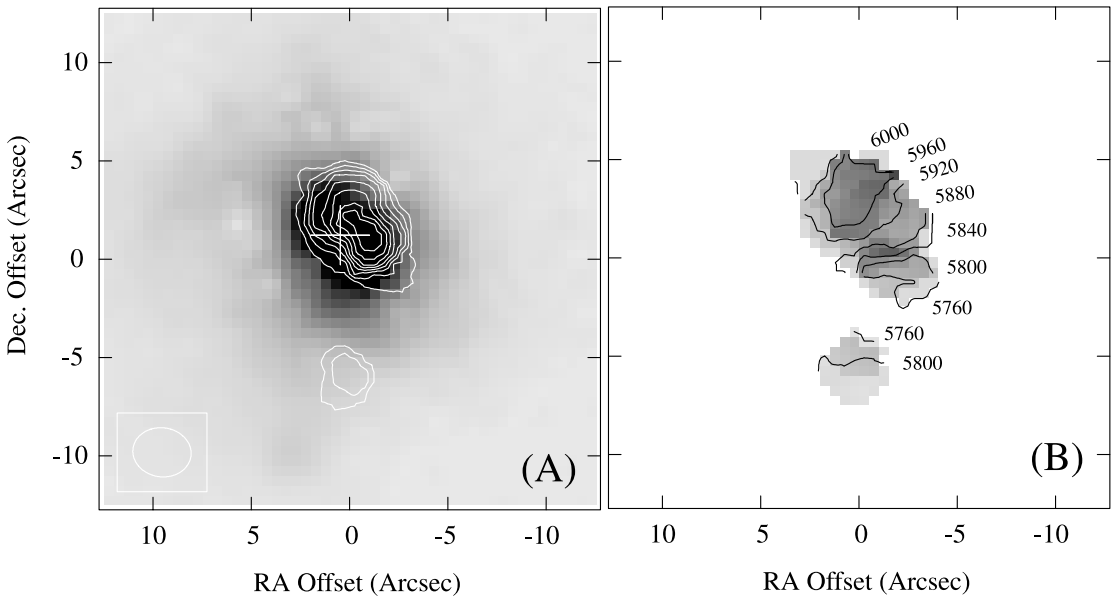

FIG. 11.—(*a*) Velocity-integrated CO (1–0) map of NGC 3921 in linear contours superposed over the Hα image. The contours are 10, 20, 30, 40, 50, 60, 70, 80, and 90 percent of the peak, which is 6.4 Jy km s^{-1} ($N_{H_2} = 3.7 \times 10^{22}$ cm^{-2}). The bulk of the 1.8×10^9 $M_\odot$ molecular gas is concentrated in a single 2 kpc diameter complex, which is clearly displaced from the optical and radio continuum peak (*plus sign*). *HST* images by Schweizer et al. (1996) reveal an abrupt change in color and an extensive array of dust filaments in the same region where the CO emission is detected (peak $A_V \sim 70$—see Fig. 12). The displacement of molecular gas from the center of the optical remnant appears real and not an extinction effect. (*b*) Mean CO velocity plotted in contours (in km s^{-1}) superposed over the velocity dispersion ("second moment") map in gray scale. The linear gray-scale range is between 0 (*white*) and 150 km s^{-1} (*black*). Unlike NGC 520 or NGC 4676A, there is no clear potential center characterized by a large velocity dispersion ($\Delta V > 100$ km s^{-1}), and evidence for reversals in the velocity field is seen.

A comparison between the gas distribution and the *Hubble Space Telescope* (*HST*) Planetary Camera (PC) image of NGC 3921 by Schweizer et al. (1996; see especially their Fig. 4) supports this picture. This comparison is shown in Figure 13, where the CO emission is contoured on the *V*-band PC image of NGC 3921 of Schweizer et al. and on the same image after a best-fit model light distribution has been subtracted. In the latter image, dust lanes show up in white, and we confirm the conclusion reached above that the main CO complex coincides with an intricate system of dust lanes concentrated mainly to the west of the nucleus. Such a displacement is unexpected since the highly dissipative nature of the cold gas should cause it to settle into the gravitational potential within an inner dynamical time of $\sim 10^7$ yr. The nonaxisymmetric appearance of the dust lanes gives the impression that the gas continues to spiral in toward the center, and the gas may be still settling within the merger potential. The combination of off-centered or "sloshing" optical isophotes (Schweizer 1996) and nonaxisymmetric dust lanes and disordered kinematics led Schweizer et al. (1996) to suggest that "on scales of order 100–1000 pc the gas and dust in NGC 3921 do not form a well-settled nuclear disk." The displaced CO appears to be a strong confirmation of this interpretation.

The molecular gas clump located to the south of the main complex lies along the ridge of optical, Hα, and H I emission that delineates the beginning of the southern tail (see Fig. 10, and also HvG96). This raises an intriguing possibility that this feature is associated with the gas-rich southern tail. Tidal features are generally very difficult to detect in CO (e.g., Smith & Higdon 1994; Smith et al. 1999), but molecular gas has been found in the bridging regions in NGC 4676 (see § 4.1.1) and in Arp 105 (Braine et al. 2000). The continued infall of gas from the outer regions might offer an explanation for the displaced molecular complex in NGC 3921 (see § 5).

4.3.2. *Molecular Gas Kinematics*

The CO channel maps for NGC 3921 are given in Figure 14. These maps show a general southwest-to-northeast velocity gradient along the main CO complex. However, numerous peaks and extensions appear and disappear in different channels at various position angles. The southwest complex appears at velocities between 5752 and 5838 km s^{-1} but with a velocity gradient opposite in sense to the main complex (i.e., decreasing velocities from south to north). The intensity-weighted mean CO velocity, shown as contours superposed over a gray-scale of the velocity dispersion map in Figure 11*b*, also show the same gradient along the main CO complex and the velocity reversal in the southwest complex. On the other hand, the local maximum in velocity dispersion characteristic of a local gravitational potential well is not seen in Figure 11*b*, supporting the conclusion reached earlier that no distinct potential maximum exists within the main molecular gas complex.

Toward the main body, the H I column density drops rapidly, and the H I tail cannot be traced as an individual kinematic structure. The H I that appears projected onto the main body is spread over a broad range of velocities, similar in width to the OVRO and single-dish profiles (~ 460 km s^{-1}, Table 2) and the stellar velocity dispersion (~ 280 km s^{-1}; Lake & Dressler 1986). Unlike the case for the other two systems, the molecular gas mass accounts for a relatively small fraction of the dynamical mass in the inner regions (about 10% and 5% inside 1 and 2 kpc radii, respectively).

The position-velocity plot of the CO data is not very informative, so we instead illustrate the CO kinematics by

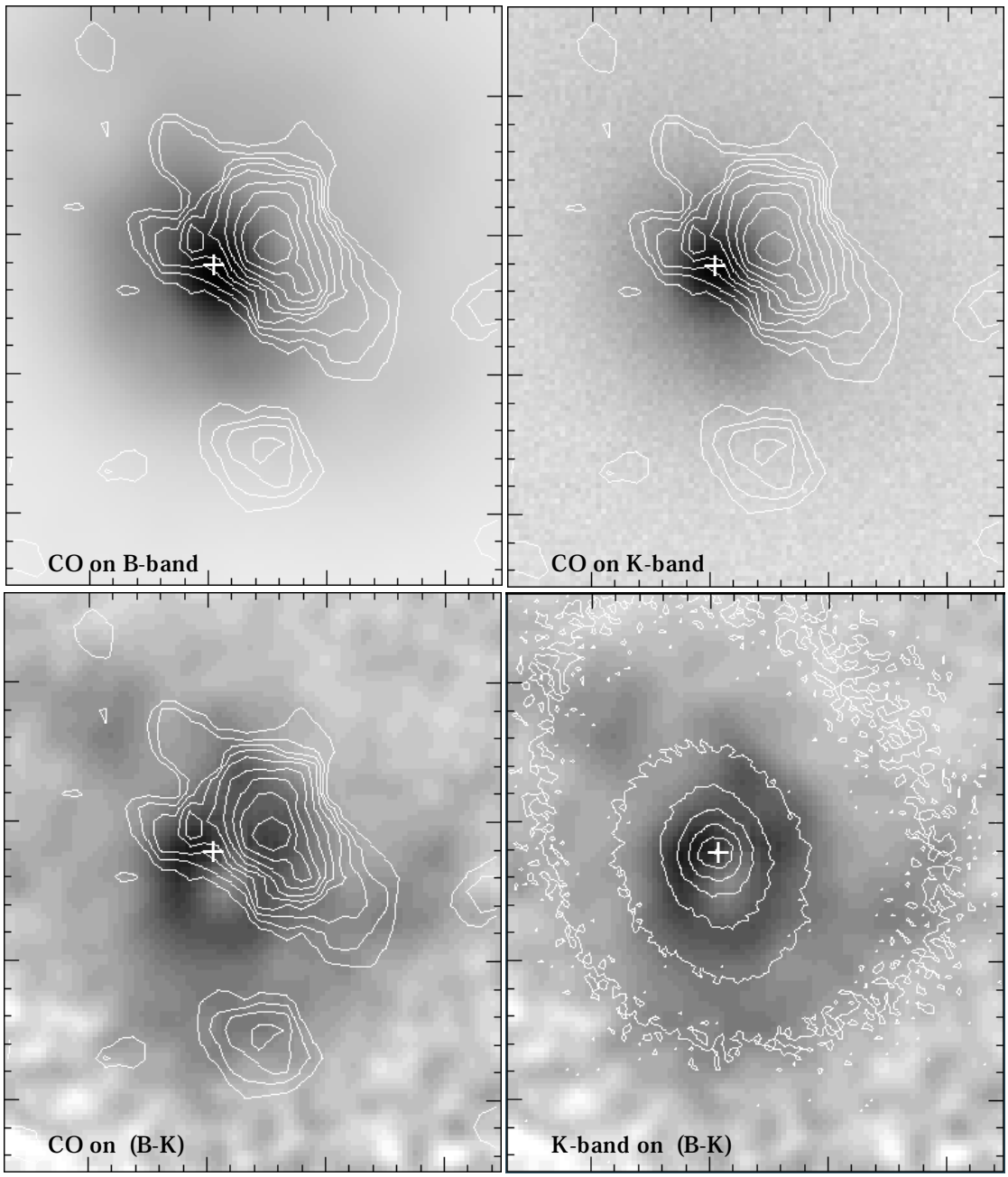

FIG. 12.—Comparisons of integrated CO emission in NGC 3921 with B, K, and $B-K$ images. A plus sign in each image marks the center of NGC 3921 as determined from the *HST* observations of Schweizer et al. (1996). The spatial offset of the central CO complex from the stellar nucleus is apparent in all continuum band images. Absence of any K-band emission coincident with the CO feature rules out the possibility of an obscured nucleus within the molecular gas complex. A spatial correspondence is found between the CO emission and the dust lanes to the northwest (darker $B-K$ colors in the lower panels). The CO is contoured at 10, 20, . . ., 90 percent of its peak value. North is toward the top and east is to the left, with vertical tick marks drawn every 1″ and horizontal tick marks drawn every 0.″1.

comparing them to the optical emission-line kinematics of S96, which were taken through a 2″ slit centered on the optical nucleus at a position angle of 45°. This comparison is presented in Figure 15. The emission-line kinematics is in general agreement with that of the CO, suggesting that the two are tracing the same feature. To the southwest, both the optical emission lines and CO show a sudden velocity reversal to lower velocities, indicating that neither component clearly traces a simple rotation about the central potential. S96 derives a systemic velocity of 5926 km s^{-1} from the emission lines, while the CO data may suggest a somewhat lower value. However, given the lack of a recognizable systematic rotational signature, we believe the data are inconclusive on this point.

The observed velocity reversals are very similar to those seen in the well-studied merger remnant NGC 7252. A comparison between the Hα (Schweizer 1982), CO (Wang et al. 1992), and tidal H I kinematics in that system (Hibbard et al. 1994; Hibbard & Mihos 1995) shows that the velocity reversals occur where tidal features are projected near the inner regions and can be explained by supposing that strong streaming motions of infalling gas from the tidal

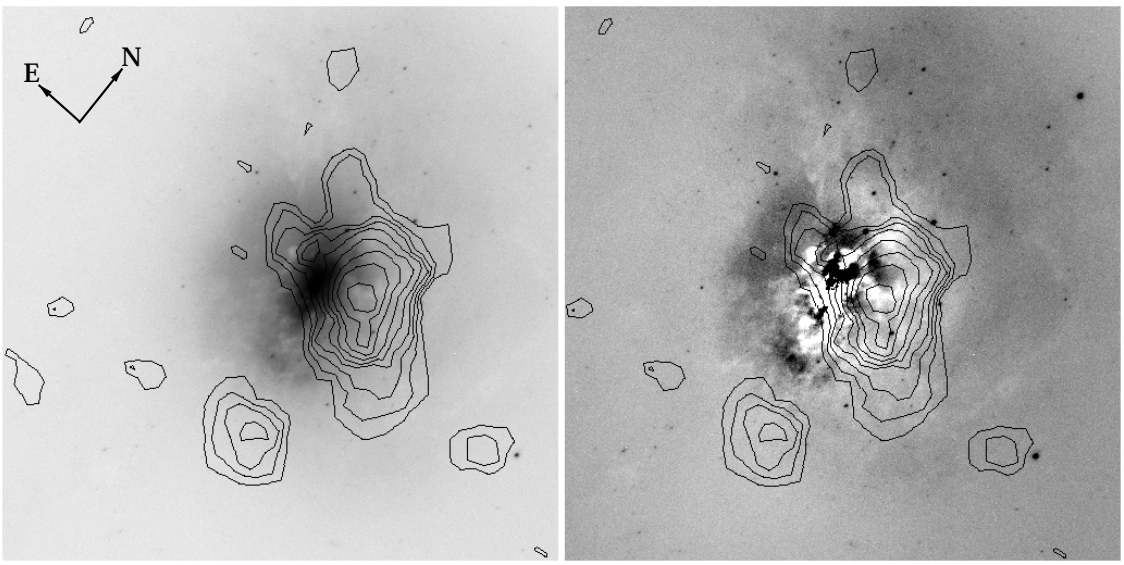

FIG. 13.—Comparisons of integrated CO emission in NGC 3921 with the *V*-band *HST* image from Schweizer et al. (1996, their Fig. 4*a*) (*left*), and with the same image, after a best-fit model light distribution has been subtracted (their Fig. 4*b*) (*right*). The region shown is approximately the same as in Fig. 12, although the field of view has been rotated. The model-subtracted image shows much more clearly the dust lanes concentrated to the west of the system, which appear white in this figure. The CO is contoured as in Fig. 12 and is seen to be very closely associated with the dust lanes to the west. The chaotic appearance of the dust lanes led Schweizer et al. (1996) to suggest that NGC 3921 is still in the process of forming a nuclear disk. The displaced CO appears to be a strong confirmation of this interpretation.

regions are superposed on the kinematics of a central molecular disk. In NGC 3921, the velocities of the southern clump (*circled S's* in Fig. 15) appear at similar velocities as the blueshifted ionized gas. These velocities are also similar to the H I velocities at the base of the southern tail (HvG96), and this kinematic component may be associated with infalling gas from the tidal regions.

In summary, the inner region of NGC 3921 has an off-center molecular gas complex that has not settled into a disk, and a second component of gas may be infalling from the tidal regions. This is rather different from the nuclear molecular complexes seen in most single-nucleus mergers, a point we will return to below.

5. DISCUSSION

The majority of mergers mapped in CO show a central molecular disk with well-defined rotational kinematics (Scoville et al. 1997; Downes & Solomon 1998; Bryant & Scoville 1999). Early gas inflow and the formation of a compact nuclear gas complex, even before the coalescence of the two stellar nuclei, are also seen in numerical studies of galaxy merger (e.g., Barnes & Hernquist 1996). This is a direct consequence of the fact that gas can shock and radiate energy away.

While some of the observed properties of these three Toomre sequence mergers follow this canonical picture of a merger involving two large spiral galaxies, significant departures are also found. A dense concentration of molecular gas is associated with the central nucleus of the late-stage merger NGC 520, but no other molecular gas concentration is detected on the second nucleus or along the region bridging the two nuclei. The formation of a compact nuclear gas complex appears to be well underway in the merging disk of NGC 4676A, but evidence for gas inflow and formation of a central gas concentration is not evident in NGC 4676B. In NGC 3921, the molecular gas complex is significantly displaced from the peak of the optical, NIR, and radio continuum emission ($\sim$760 pc).

One possible explanation for these departures from the canonical merger scenario is that one or both progenitor disks of these optically selected merger systems may have been relatively gas-poor. Based on the analysis of the stellar and H I tidal features, Hibbard & van Gorkom (1996) suggest that both NGC 520 and NGC 3921 are the products of an encounter between one gas-rich disk and one gas-poor system, such as an S0 or Sa galaxy (e.g., Thronson et al. 1989).

This suggestion for NGC 3921 is further supported by the observations of Schweizer et al. (1996), who find many fewer young globular clusters in this system compared with the gas-rich mergers NGC 4038/39 and NGC 7252. The absence of molecular gas directly associated with the second nucleus of NGC 520 and the stellar nucleus of NGC 3921 is then explained naturally if little molecular gas has been funneled into the nuclei during the merger process. The absence of gas in one progenitor also lessens the frequency of gas cloud collisions in the second disk, especially within the central few kiloparsecs (Olson & Kwan 1990), and therefore less dissipation and angular momentum transport are expected.

The presence of two large, atomic gas–rich tidal tails associated with NGC 4676 suggests that both progenitor disks were gas-rich (see HvG96), and a different explanation may be needed. As stated earlier, NGC 4676B appears to be an early Hubble type spiral and may also have been relatively molecularly gas-poor initially. A numerical study by Mihos & Hernquist (1996) has shown that the presence or absence of a massive bulge in the progenitor disk can produce a large difference in the evolution of the gas distribution and kinematics, the peak gas density achieved, and the resulting star formation activity. The apparent difference between the current molecular gas content in the

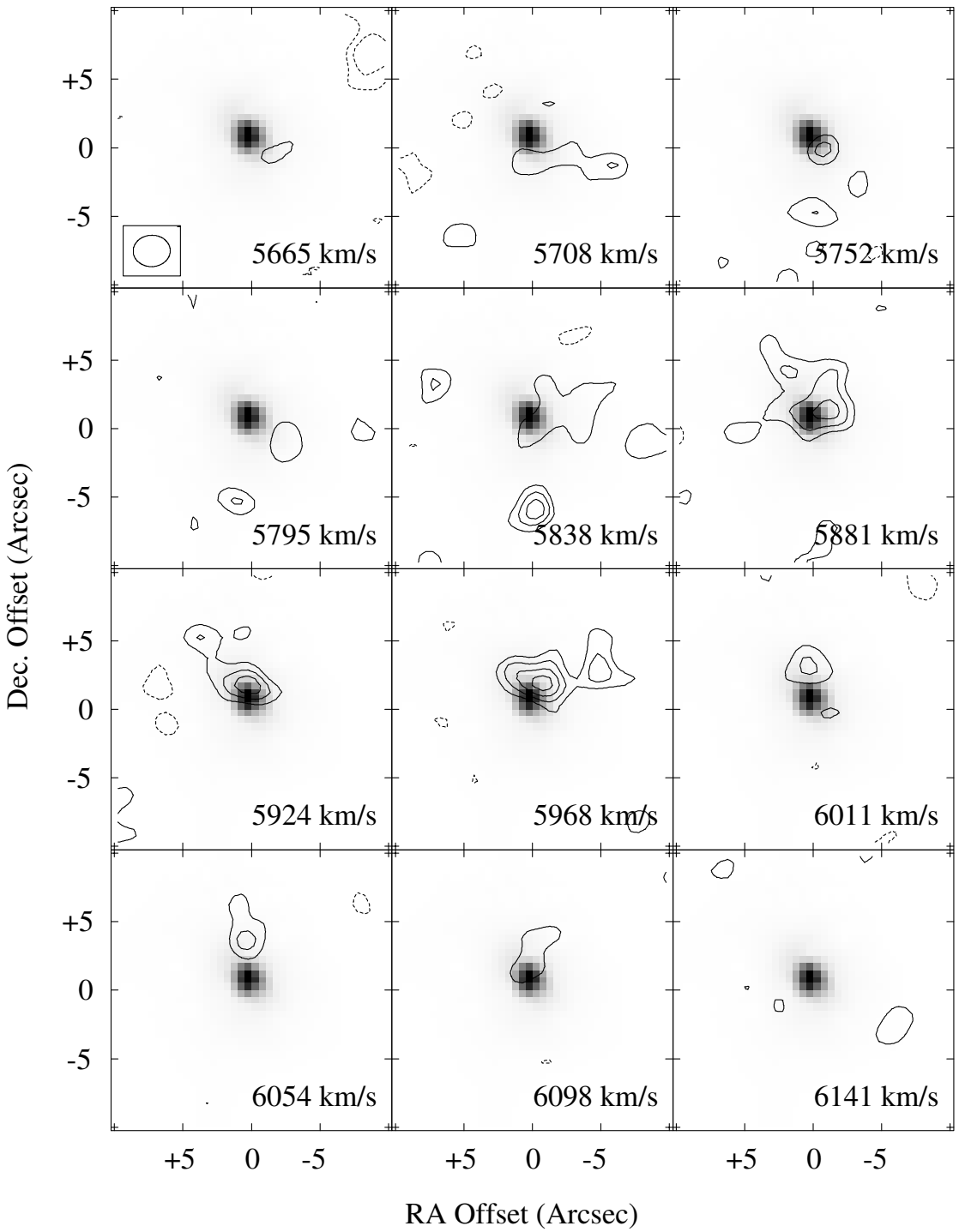

FIG. 14.—Individual channel maps of CO (1–0) emission in NGC 3921 with 2.″3 × 2.″7 (0.87 × 1.0 kpc, P.A. = 83°) resolution shown in 41.6 km s^{-1} velocity increments contoured on a gray-scale representation of the Hα image. The brightest peak (42.1 mJy $beam^{-1}$) corresponds to a brightness temperature of 0.64 K averaged over the beam area. The contour levels are −3, −2, +2, +3, +4, and +5 times 8 mJy $beam^{-1}$ (1 σ). CO emission occurs clearly displaced to the northwest of the radio nucleus, and the gas kinematics is more complex than a simple rotation.

two merging disks in NGC 4676 may be explained more naturally by differences in the internal structure of the progenitors.

While it is significant that these three optically selected mergers show notable departures from the canonical merger scenario, we should also keep in mind that they nevertheless represent only three individual snapshots of their respective merger evolutions. For example, the apparent difference in the status of molecular gas between the two merging disks in NGC 4676 may simply reflect a slight delay in the onset of the gas inflow created by the difference in the spin-orbit coupling, however fortuitous this may seem. Similarly, NGC 3921 may be in a brief, early stage in its merger evolution and may soon develop a molecular disk. Schweizer (1996) has also presented observation evidence that NGC 3921 is a dynamically young merger.

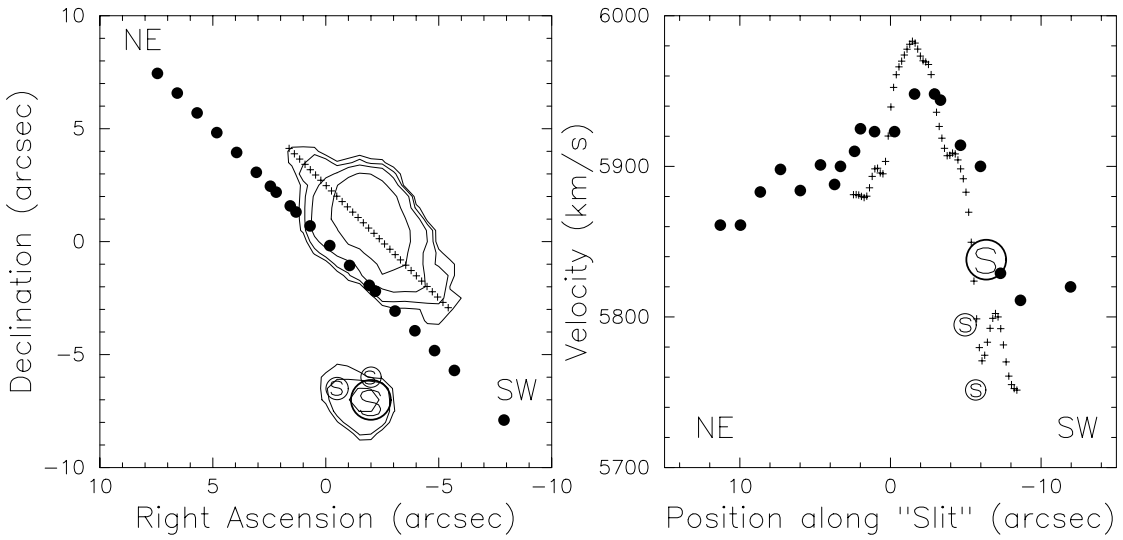

FIG. 15.—*Right*, position-velocity plot of CO emission in NGC 3921 in comparison with the kinematics of the optical emission lines; *left*, actual positions of each sampled component. The Hα kinematics of S96 is indicated by filled circles. CO velocities measured from the first moment map across the peak of the CO distribution at a P.A. of 45° and are shown as small plus signs. The "clean components" associated with the southern clump are denoted by circled S's. The size of the symbol is proportional to the S/N of the component.

However, central CO disks are commonly found in both earlier (e.g., NGC 520 and NGC 4676A) and later stage (e.g., NGC 7252) mergers. One may further postulate that NGC 3921 represents a stage even further in its evolution where the original central gas complex is already dispersed. In this scenario, the observed gas in the central region is largely the result of recent inflow from the tidal tails (see Hibbard & Mihos 1995).

Finally, a clear and significant quantitative result from this imaging study of optically selected merger systems is that their central molecular gas surface density is systematically smaller by orders of magnitude compared with the IR-selected mergers (see Table 2). Further, the level of activity associated with each of the merger systems appears to depend strongly on the central gas density. We will discuss this and other comparisons of global properties between the optically selected and IR-selected mergers in a separate paper (Paper II).

6. SUMMARY

In an effort to better understand the nature of the luminous IR galaxy phenomenon and to scrutinize the details of the merger scenario, we have mapped the CO emission in an optically selected sample of ongoing mergers with moderate IR luminosity ("Toomre sequence"; Toomre 1977) at a resolution and sensitivity comparable to those of the more IR-luminous objects, and the response of the molecular gas material deep inside the potential of the colliding galaxies is traced. The summary of our findings is as follows.

1. A compact ($R \leq 2$ kpc) molecular complex is found well centered on the inner stellar disk of NGC 4676A, forming a disklike or a ringlike structure with the regular kinematics consistent with simple rotation. This molecular gas concentration contributes a significant fraction (20%) of the total mass in the nuclear region. The CO emission occurs along the 7 kpc stellar bar in NGC 4676B. The surface brightness of the CO emission is extremely low, and tapering the data from 3″ to 5″ resolution nearly doubles the detected flux.

2. Nearly all of the CO emission detected at the primary nucleus position in NGC 520 is concentrated in a 1 kpc diameter ringlike structure, coincident with the extended radio continuum source mapped by Condon et al. (1990). The derived H_2 mass and the dynamical mass are comparable, and the gas mass must constitute a large fraction of the total mass in the nuclear starburst region. No CO emission is detected on the second nucleus in NGC 520.

3. The molecular gas distribution in NGC 3921 is quite different from any other singly nucleated merger mapped in CO. The CO emission is significantly displaced from the peak of the optical, NIR, and radio continuum emission ($\sim$760 pc), and both the distribution and kinematics suggest that the molecular gas has not settled into the new remnant potential. The molecular gas complex contributes a minor fraction ($\lesssim$10%) of the dynamical mass in the inner regions.

4. Molecular gas clouds are detected outside the central regions of NGC 3921 and NGC 4676. They may be associated with the tidal tails and bridges mapped in H I.

5. A consistent trend of anticorrelation is seen between CO and Hα emission in NGC 520 and NGC 4676A, and the large extinction inferred from the CO emission ($A_V = 600$ and 120) suggests that the intense nuclear starburst regions in these galaxies are completely obscured. This finding offers a natural explanation for the severe underestimation of the star formation rate by optical tracers compared with the IR (e.g., Bushouse et al. 1988; Kennicutt 1989, 1998).

6. Departures from the canonical scenario for a merger involving two large spiral galaxies are found in all three Toomre sequence mergers studied. A relatively gas-poor progenitor, as inferred from the optical and H I observations by HvG96, offers a possible explanation for NGC 520 and NGC 3921. A gas-poor progenitor disk or rapid evolution in gas content by some dynamical process (i.e., Mihos & Hernquist 1996) may offer a plausible explanation for the low molecular gas density in NGC 4676B.

7. The central molecular gas density in these optically selected mergers is systematically smaller by an order of magnitude compared with the IR-selected mergers; the level

of activity associated with each of the merger systems appears to depend strongly on the central gas density. This and other detailed comparisons of global properties between the optically selected and IR-selected mergers will be presented in Paper II.

The authors thank F. Combes for discussing the results of her IRAM 30 m CO (1–0) observations of NGC 3921 prior to publication and allowing us to show the spectrum in Figure 1 and F. Schweizer for sending us his Hα kinematic data on NGC 3921 and for a critical reading of an earlier version of this manuscript. We thank J. Barnes, M. Rupen, N. Scoville, J. van Gorkom, and J. Wang for useful discussions. We also thank the anonymous referee, whose helpful suggestions improved this manuscript. This research was supported in part by NSF grant AST 93-14079. The National Radio Astronomy Observatory is a facility of the National Science Foundation operated under cooperative agreement by Associated Universities Inc.

REFERENCES

Arp, H. 1966, ApJS, 14, 1
Barnes, J. E. 1998, in Galaxies: Interactions and Induced Star Formation, Saas-Fee Advanced Course No. 26, ed. R. C. Kennicutt, Jr., F. Schweizer, & J. E. Barnes (Berlin: Springer), 275
Barnes, J. E., & Hernquist, L. 1991, ApJ, 370, L65
———. 1992, ARA&A, 30, 705
———. 1996, ApJ, 471, 115
Binney, J., & Tremaine, S. 1987, Galactic Dynamics (Princeton: Princeton Univ. Press), chap. 2
Braine, J., Lisenfeld, U., Duc, P.-A., & Leon, S. 2000, Nature, 403, 867
Bryant, P. M., & Scoville, N. Z. 1996, ApJ, 457, 678
———. 1999, AJ, 117, 2632
Bushouse, H. A., Werner, M. W., & Lamb, S. A. 1988, ApJ, 335, 74
Carilli, C. L., Wrobel, J. M., & Ulvestad, J. S. 1998, AJ, 115, 928
Casoli, F., Boissé, P., Combes, F., & Dupraz, C. 1991, A&A, 249, 359
Condon, J. J., Helou, G., Sanders, D. B., & Soifer, B. T. 1990, ApJS, 73, 359
Cram, L., Hopkins, A., Mobasher, B., & Rowan-Robinson, M. 1998, ApJ, 507, 155
Downes, D., & Solomon, P. M. 1998, ApJ, 507, 615
Helou, G., Khan, I. R., Malek, L., & Boehmer, L. 1988, ApJS, 68, 151
Hibbard, J. E., Guhathakurta, P., van Gorkom, J. H., & Schweizer, F. 1994, AJ, 107, 67
Hibbard, J. E., & Mihos, J. C. 1995, AJ, 110, 140
Hibbard, J. E., & van Gorkom, J. H. 1996, AJ, 111, 655 (HvG96)
Kenney, J. D. P., Wilson, C. D., Scoville, N. Z., Devereux, N. A., & Young, J. S. 1992, ApJ, 395, L79
Kennicutt, R. C., Jr. 1989, ApJ, 344, 685
———. 1998, ARA&A, 36, 189
Lake, G., & Dressler, A. 1986, ApJ, 310, 605
Landolt, A. U. 1983, AJ, 88, 439
———. 1992, AJ, 104, 340
Lo, K. Y., Cheung, K. W., Masson, C. R., Phillips, T. G., Scott, S. L., & Woody, D. P. 1987, ApJ, 312, 574
Mihos, J. C., Bothun, G. D., & Richstone, D. O. 1993, ApJ, 418, 82
Mihos, J. C., & Hernquist, L. 1996, ApJ, 464, 641
Negroponte, J., & White, S. D. M. 1983, MNRAS, 205, 1009
Olson, K. M., & Kwan, J. 1990, ApJ, 361, 426
Sanders, D. B., & Mirabel, I. F. 1996, ARA&A, 34, 749
Sanders, D. B., Scoville, N. Z., Sargent, A. I., & Soifer, B. T. 1988, ApJ, 324, L55
Sanders, D. B., Scoville, N. Z., & Soifer, B. T. 1991, ApJ, 370, 158
Sanders, D. B., Solomon, P. M., & Scoville, N. Z. 1984, ApJ, 276, 182
Schweizer, F. 1982, ApJ, 252, 455
———. 1996, AJ, 111, 109 (S96)
Schweizer, F., Miller, B. W., Whitmore, B. C., & Fall, S. M. 1996, AJ, 112, 1839
Scoville, N. Z., Carlstrom, J. C., Chandler, C. J., Phillips, J. A., Scott, S. L., Tilanus, R. P., & Wang, Z. 1993, PASP, 105, 1482
Scoville, N. Z., Yun, M. S., & Bryant, P. M. 1997, ApJ, 484, 702
Shen, J. J., & Lo, K. Y. 1995, ApJ, 450, L39
Shepherd, M. C., Pearson, T. J., & Taylor, G. B. 1994, BAAS, 26, 987
Smith, B. J., & Higdon, J. L. 1994, AJ, 108, 837
Smith, B. J., Struck, C., Kenney, J. D. P., & Jogee, S. 1999, AJ, 117, 1237
Solomon, P. M., Downes, D., & Radford, S. J. E. 1992, ApJ, 387, L55
Stanford, S. A., & Balcells, M. 1990, ApJ, 355, 59
Stanford, S. A., Sargent, A. I., Sanders, D. B., & Scoville, N. Z. 1990, ApJ, 349, 492
Stockton, A. 1974, ApJ, 187, 219
Stockton, A., & Bertola, F. 1980, ApJ, 235, 37
Thronson, H. A., et al. 1989, ApJ, 344, 747
Toomre, A. 1977, in The Evolution of Galaxies and Stellar Populations, ed. B. M. Tinsley & R. B. Larson (New Haven, CT: Yale Univ. Press), 401
Toomre, A., & Toomre, J. 1972, ApJ, 178, 623
Wainscoat, R. J., & Cowie, L. L. 1992, AJ, 103, 332
Wang, Z., Schweizer, F., & Scoville, N. Z. 1992, ApJ, 396, 510
Wilson, C. D., Scoville, N., Madden, S. C., & Charmandaris, V. 2000, ApJ, 542, 120
Young, J. S., & Knezek, P. M. 1989, ApJ, 347, L55
Young, J. S., & Scoville, N. Z. 1991, ARA&A, 29, 581
Young, J. S., et al. 1995, ApJS, 98, 219
Yun, M. S., & Hibbard, J. E. 2001, ApJ, submitted (Paper II)